Authors' Accepted Manuscript
Paper published in Fuel, Volume 340, 2023, 127523 © 2023 Elsevier Ltd. https://doi.org/10.1016/j.fuel.2023.127523

Adsorptive desulphurization of model and real fuel via wire-, rod-, and flower-like Fe_3O_4@MnO_2@activated carbon made from palm kernel shells as newly designed magnetic nanoadsorbents

Ibrahim Sh. Ali[a], Omer Yasin Thayee Al-Janabi[b*], Emaad T. B. Al-Tikrity[c], Peter J. S. Foot[d]

[a,c]College of Science, Industrial Chemistry laboratory research, Tikrit University, Salah Aldeen, Tikrit 34001, Iraq

[b]College of Petroleum Process Engineering, Petroleum & Gas Refining Engineering, Tikrit University, Salah Aldeen, Tikrit 34001, Iraq

[d]Kingston University London, School of LSPC, Kingston upon Thames KT1 2EE (UK)

*corresponding author: omaroilgas@tu.edu.iq

Abstract

The removal of organic sulphur from liquid fuel *via* applicable and cheap processes is one of the most challenging energy issues worldwide. Adsorptive desulphurization (ADS) processes can address this issue if highly effective magnetic nanoadsorbents with favourable textural properties are used. In this work, activated carbon produced from palm kernel shells was decorated with wire-, rod-, and flower-like magnetic MnO_2 by a hydrothermal route to produce reusable magnetic nanoadsorbents with tunable pore volume and pore diameter. The magnetic nanoadsorbents labelled Fe_3O_4@MnO_2-w@AC, Fe_3O_4@MnO_2-r@AC and Fe_3O_4@MnO_2-f@AC were characterized using state-of-the-art spectroscopic techniques and used for sulphur removal from model and real fuels. The results revealed that the prepared magnetic nanoadsorbents had suitable oxygen functionalities, porous morphology and specific surface area of 480 for wire, 312 for rod, and 340 m^2 g^{-1} for flower-like magnetic nanoadsorbents. The newly-designed magnetic nanoadsorbents exhibited superior sulphur removal efficiency at 100 min contact time, 35°C adsorption temperature, and 0.4 g adsorbent dose per 40 mL of model or real fuel. Among them, a wire-like magnetic nanoadsorbent showed 99% sulphur removal from model fuel with 530 ppm sulphur content as DBT, 97.6% and 90% sulphur removal from commercial kerosene and diesel fuels with 430 and 1050 ppm sulphur content, respectively. The adsorption kinetics, isotherms and thermodynamics disclosed that adsorption of organic sulphur follows the pseudo-first order kinetic model, was an exothermic, and diffusion-controlled process. The magnetic properties enabled the nanoadsorbents to be recovered more easily and reused at least five times.

Keywords: polymorph magnetic manganese dioxide; Activated carbon; Adsorption; Sulphur removal; commercial fuel.

Paper published in Fuel, Volume 340, 2023, 127523 https://doi.org/10.1016/j.fuel.2023.127523

1. Introduction

Sulphur-containing compounds from fossil fuels have recently emerged as a disturbing environmental concern because of the harmful emissions from diesel powered vehicles. The organic sulphur compounds present are mainly converted into SO_3, which readily dissolves in water vapour to form sulphuric acid. The generated sulphuric acid is then changed into fine particles that can enter human lungs and cause lung cancer [1-4]. Furthermore, the presence of sulphur compounds in petroleum products causes corrosion problems in petroleum refinery equipment and poisons downstream catalysts [5-8]. As a result, additional rigorous environmental rules on the allowable sulphur limit (ppm) to lower the S content in transportation fuels are continually being introduced by governments [9-12]. Reducing the harmful effects of sulphur emissions is often achieved through decreasing the emission rates of SO_3, and/or manufacturing ultra-low sulphur content fuels [13-15]. The traditional hydrodesulphurization (HDS) method is generally effective for open-chain and acyclic S-compounds and less effective for benzothiophene (BT), dibenzothiophene (DBT) and their derivatives. The HDS process requires severe conditions (temperatures up to 400°C and high pressures up to 10 MPa) and extremely durable catalysts [16]. To achieve ultra-deep desulfurization, various non-HDS technologies like adsorptive desulfurization (ADS), extractive desulfurization (EDS) oxidative desulfurization (ODS) and biodesulfurization (BDS) are considered to be the most advanced techniques [17-20]. Among the various non-HDS technologies, ADS is regarded as one of the most promising methods and has attracted wide attention because of advantages like low cost, mild operating conditions and low energy consumption, as there is no need for hydrogen or oxygen inputs [21-23]. The efficiency of ADS depends mostly on the adsorbent's textural characteristics such as high surface area and pore volume, more mesopores and surface-active sites and good structural strength and stability [24]. Many studies on ADS of transportation fuels have been carried out by using activated carbon [25], mesoporous materials, zeolites [26], metal oxides [27] and metal-organic frameworks (MOFs) as adsorbents [28].

Metal oxide-based adsorbents were studied for ADS since they possess many attractive features such as simple synthesis routes, good structural stability and insolubility in common solvents [29, 30]. Among them, manganese dioxide nanoparticles and MnO_2-based nanocomposites were concluded to be good candidates for environmental remediation and energy storage owing to their low cost, high surface area, eco-friendly nature and wide structural diversity, combined with ideal physical and chemical properties [31-33]. Manganese dioxide NPs and manganese dioxide-based nanocomposites have been synthesized via hydrothermal, thermal degradation, sol-gel, electro-deposition and microwave-assisted routes [34-37]. Synthesizing manganese dioxide with nanowire, nanorod, nanoflake, nanotube, nano-sheet or nanoflower morphologies, can bring the following benefits to

nanostructured materials: increasing the specific surface area; boosting the formation of oxygen vacancies and surface defects; facilitating mass-transfer and light harvesting; and quickening charge transfer and improving the separation efficiency of electron-hole pairs [38-43]. Researchers have extensively investigated MnO_2 NPs and MnO_2-based nanocomposites for diverse applications such as heavy metal and organic pollutant removal, air purification and microwave absorption [42, 43].

Yaseen et al. [5] fabricated a nanoadsorbent composed of Zn- and Mn-loaded activated carbon (AC) derived from corn cobs for the adsorptive desulfurization of model and real fuel oils. Preliminary adsorption experiments were accomplished with 0.15 g adsorbent dosage, 2h contact time at 30°C, which removed 95.7% of dibenzothiophene (DBT) from 10 mL model fuel containing 200 ppm DBT, 92% and 50% sulphur removal from kerosene and gasoline fuels, respectively. Saleh et al. [6] successfully treated activated carbon with manganese oxide to improve its surface properties for adsorptive desulfurization. The adsorbent displayed oxygen-containing functional groups and distinctive pore structures that enabled rapid uptake of 4.5 mg g^{-1}, 5.7 mg g^{-1} and 11.4 mg g^{-1} for simultaneous adsorption of thiophene, benzothiophene and dibenzothiophene in a batch process. Magnetic Fe_3O_4@MnO_2 core-shell nanoflower attached to Aspergillus niger carbon microtube was designed by Yang et al. [44] as a highly efficient, recyclable and environmentally-friendly adsorbent for the removal of heavy metals from synthetic wastewater. Due to the synergistic effects of the high adsorption capacity of MnO_2, the magnetism of Fe_3O_4 and large pore size of Aspergillus niger carbon, the adsorbent achieved an extremely high adsorption capacity of 934 mg g^{-1} and a shorter adsorption time of 5 min using 20 mL synthetic wastewater containing 1000 ppm heavy metal ions. Maneechakr and Mongkollertlop [45] systematically investigated the adsorption behaviour of heavy metal cations such as Cd^{2+}, Cr^{3+}, Pb^{2+} and Hg^{2+} using active MnO_2-modified magnetic carbonized biochar powder (CP-Fe) derived from palm kernel cake residue. The adsorption performance of (CP-Fe) was efficiently improved by doping with $KMnO_4$ (CP-Fe-Mn). The maximum adsorption capacities (q_{max}) for Cd^{2+}, Cr^{3+}, Pb^{2+} and Hg^{2+} were 18.60, 19.92, 49.64 and 13.69 mg g^{-1}, respectively.

Despite all the interest in manganese dioxide NPs and MnO_2-based nanocomposites, to our best information, the use of magnetic MnO_2 nanocomposites with different MnO_2 morphologies as nanoadsorbent for adsorptive desulphurization of liquid fuel has not previously been reported. Therefore in the present study, wire-, rod-, and flower-like magnetic MnO_2 NPs decorated activated carbon produced from palm kernel shells have been synthesized by a hydrothermal method and evaluated as promising green magnetic nanoadsorbents for sulphur removal from model and commercial fuels. In this study, we employed activated carbon as the substrate for its large specific surface area and abundant oxygen-containing groups. Using a hydrothermal method, different

Paper published in Fuel, Volume 340, 2023, 127523 https://doi.org/10.1016/j.fuel.2023.127523

morphologies of magnetic MnO_2 NPs were deposited on the surface of the activated carbon sheets. The magnetic property of our synthesized nanoadsorbents provides an effective approach for rapid separation and recovery of the nanoadsorbent for recycling. The surface chemistry and crystallinity of the prepared magnetic nanoadsorbents was studied by powder X-ray diffractometry (XRD) and by Fourier Transformer Infrared spectroscopy (FTIR), Raman spectroscopy and energy-dispersive X-ray analysis (EDAX) elemental mapping. Field emission scanning electron microscopy (FESEM) was used to investigate surface morphology, while particle sizes were inspected by transmission electron microscopy (TEM). The Brunauer-Emmett-Teller (BET) method was used to determine the specific surface area, and the pore size distribution and pore volume of the prepared magnetic nanoadsorbents were calculated using the Barret-Joyner-Halenda (BJH) model. Magnetic properties were investigated by vibrating scanning magnetometer (VSM). The adsorptive desulphurization of model and commercial fuels was carried out in a batch system using a glass reactor vessel. The ADS process was optimized in terms of contact time, sulphur concentration, adsorbent dose, and temperature. The optimum ADS conditions were considered for adsorptive desulphurization of kerosene and diesel as commercial fossil fuels. Adsorption kinetics, adsorption isotherms and adsorption thermodynamic of the prepared materials were all thoroughly investigated.

2. Experimental and methods

2.1. Materials

All the chemicals and reagents used in this work were of analytical grade 97-99% purity, so they were not purified further. Milli-Q water (resistivity greater than 18.2 MΩ.cm) was used during the synthesis steps. Potassium permanganate ($KMnO_4$) (99%), manganese sulphate monohydrate $MnSO_4.H_2O$ (99%) were purchased from Sigma Aldrich. Iron chlorides $FeCl_3.6H_2O$ (97%) and $FeCl_2.4H_2O$ (99%) were purchased from Fluka and Glentham, respectively. Hydrochloric acid (37 wt%) and ammonia solution (25 wt%), and n-decane (GC grade) were purchased from Merck.

2.2. Synthesis of Fe_3O_4 NPs

A coprecipitation route was used to synthesize the Fe_3O_4 NPs [46]. In a typical reaction, 9.46 mmol of $FeCl_2.4H_2O$ and 18.92 mmol of $FeCl_3{\cdot}6H_2O$ were dissolved in 60 mL distilled water and ultrasonicated for 30 min at 50°C in N_2 atmosphere. Later, 35 mL ammonia solution (25 wt%) was injected into the reaction flask over 90 min to maintain slow coprecipitation throughout Fe_3O_4 nuclei formation. In order to grow Fe_3O_4 particles with a spherical shape and control the particle size, the pH value of the reaction solution was kept within a range of about 10-12. After completing the addition of ammonia solution, the reaction mixture was continuously ultrasonicated for another 60 min at 50°C in N_2 atmosphere to complete the Fe_3O_4 NPs growth. The black as-prepared products were separated by a small magnetic bar, washed several times with distilled water/ethanol mixture

Paper published in Fuel, Volume 340, 2023, 127523 https://doi.org/10.1016/j.fuel.2023.127523

and then dried at 50°C for 9h in vacuum. Finally, the black dried particles (32-46 nm size, see Fig. S1a in supporting information file) of Fe_3O_4 NPs were obtained.

2.3. Preparation of MnO_2 nanoparticles with different morphologies

Wire-, rod- and flower-like MnO_2 NPs were synthesized following certain methodologies [42, 47, 48,]. The wire-like MnO_2 was synthesized as follows: 1.5 g $KMnO_4$ and 0.275 g $MnSO_4.H_2O$ were dissolved in 80 mL deionized water. After stirring for 30 min, the mixture was transferred into a 100 mL Teflon-lined autoclave and the reaction proceeded for 24h at 240°C. Thereafter, the product was washed several times with deionized water and absolute ethanol and separated by centrifuge (10000 rpm). The collected solid labelled MnO_2-w NPs was dried for 24h at 60°C, and then sealed for further use and characterization.

The rod-like MnO_2 NPs labelled MnO_2-r was synthesized as follows: 0.3214 g $KMnO_4$ was dissolved in 30 mL deionized water, and 0.7 mL of 37 wt% HCl were added to the mixed solution. After stirring for 30 min, the mixture was transferred to a 100 mL Teflon-lined autoclave and reacted for 12h at 140°C. Later, the product was collected, and the next steps were the same as for MnO_2-w NPs.

The flower-like MnO_2 NPs labelled MnO_2-f was synthesized as follows: 0.51 g $KMnO_4$ was first dissolved in 35 mL deionized water, and 0.7 mL of 37 wt% HCl was then added dropwise. After stirring for 30 min, the mixture was transferred to a 100 mL Teflon-lined autoclave and reacted for 6h at 110°C. The rest of the procedures were the same as for MnO_2-w NPs.

2.4. Preparation of wire-, rod-, and flower-like magnetic MnO_2 nanoparticles

Wire-, rod- and flower-like magnetic MnO_2 nanoparticles NPs were synthesized following a typical reaction procedure [44]. The Fe_3O_4@MnO_2-w NPs was synthesized as follows: 0.3 g Fe_3O_4 NPs previously prepared, 1.5 g $KMnO_4$, 0.275 g $MnSO_4.H_2O$, and 0.7 mL of 37 wt% HCl were uniformly dispersed in 80 mL of deionized water and ultrasonicated for 30 min using a probe sonicator. Thereafter, the mixture was transferred into a 100 mL Teflon-lined autoclave and reacted for 24h at 240°C. Finally, the Fe_3O_4@MnO_2-w precipitate was collected by magnet and washed with ethanol and water several times, followed by freeze-drying under vacuum for 24h for further use and characterization.

The Fe_3O_4@MnO_2-r NPs was synthesized as follows: 0.3 g Fe_3O_4 NPs, 1.5 g $KMnO_4$ and 0.7 mL of 37 wt% HCl were uniformly dispersed into 80 mL of deionized water and ultrasonicated for 30 min using a probe sonicator. The mixture was then transferred into a 100 mL Teflon-lined autoclave and reacted for 12h at 140°C. The Fe_3O_4@MnO_2-r precipitate was collected by magnet and washed with ethanol and water several times, followed by freeze-drying under vacuum for 24h for further use and characterization.

Paper published in Fuel, Volume 340, 2023, 127523 © 2023 Elsevier Ltd. https://doi.org/10.1016/j.fuel.2023.127523

The Fe_3O_4@MnO_2-f NPs was synthesized as follows: 0.3 g Fe_3O_4 NPs, 1.5 g $KMnO_4$ and 0.7 mL of 37 wt% HCl were uniformly dispersed in 80 mL of deionized water and ultrasonicated for 30 min using a probe sonicator. The mixture was transferred into a 100 mL Teflon-lined autoclave and reacted for 6h at 110°C. Finally, the Fe_3O_4@MnO_2-f precipitate was collected by magnet and washed with ethanol and water several times, followed by freeze-drying under vacuum for 24h for further use and characterization.

2.5. Preparation of activated carbon from palm kernel shells

The palm kernel shells PKS were locally collected to be used as the precursor for the activated carbon production *via* physicochemical approach (see Fig.1) [49, 50]. The collected PKS were thoroughly cleaned using deionized water, then crushed into powder using a grinding machine and dried at 100°C in an oven. The dried PKS were thermally carbonized under N_2 flowrate at 500°C and heating rate of 10°C min^{-1} in a calcination furnace for 2h to remove the small amount of organic molecules. Thereafter, to improve the specific surface area, the pre-carbonized PKS were chemically activated by dipping in 20 wt.% KOH aqueous solution and then stirred vigorously for one day to ensure complete infiltration. Subsequently, the mixture was annealed at 900°C for 2h under N_2 flow. The product was crushed using a mortar and pestle, washed with 1M HCl and rinsed with excess of deionized water to obtain a neutral pH. The cleaned sample was oven-dried at 100°C for 24h to remove any internal moisture, then weighed. kept in a vial and labelled as porous activated carbon (PAC) for further use and analyses.

2.6. Preparation of wire-, rod-, and flower-like Fe_3O_4@MnO_2 decorated activated carbon

In a typical reaction, the as-prepared PAC powder (1 g) was re-dispersed in 60 mL deionized water ultrasonically for 90 min. Then, Fe_3O_4@MnO_2-w (15 wt%) was added to the dispersion and the system was ultrasonicated for another 60 min. The mixture was then transferred to a 100 mL Teflon-lined autoclave and maintained at 100ºC for 5h. After cooling to room temperature, the obtained magnetic nanoadsorbent, labelled Fe_3O_4@MnO_2-w@AC, was washed with deionized water, collected by magnet, and then dried in a vacuum oven at 35ºC for 12h. The Fe_3O_4@ MnO_2-r@AC and Fe_3O_4@ MnO_2-f@AC magnetic nanoadsorbents were prepared by following the same procedure as for Fe_3O_4@ MnO_2-w@AC.

Authors' Accepted Manuscript
Paper published in Fuel, Volume 340, 2023, 127523 © 2023 Elsevier Ltd. https://doi.org/10.1016/j.fuel.2023.127523

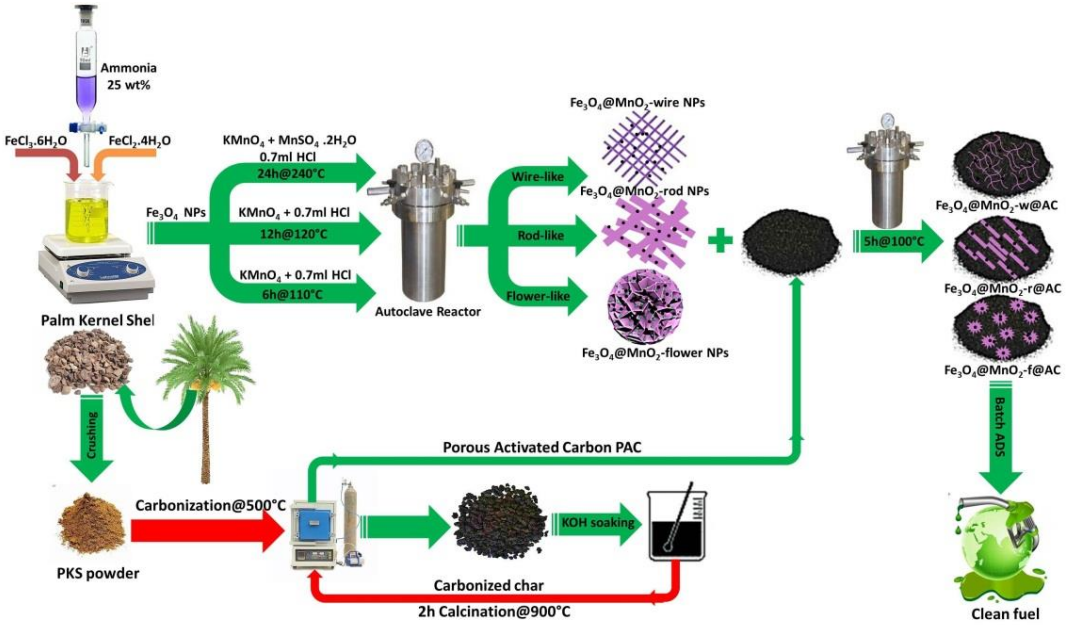

Fig. 1. Hydrothermal synthesis of magnetic nanoadsorbents.

2.7. Materials characterization

The newly-synthesized magnetic nanoadsorbents were characterized by FTIR Spectroscopy on a model Shimadzu 8400 spectrophotometer in the 400-4000 cm^{-1} range, and elemental mapping analysis was done by energy-dispersive X-ray spectroscopy (EDAX) (ZEISS Sigma 300). Raman spectra of the nanoadsorbents were monitored in the region of 100-3600 cm^{-1}. The crystalline structures of the synthesized materials were examined by X-ray powder diffractometry (XRD) (Shimadzu XRD-6000) using Cu Kα radiation (λ = 1.5406 Å), 10°-80° 2θ, and 5 degrees/s scan rate. The crystallite size (D) of the prepared materials was calculated from the width of the most intense peak using the Debye-Scherrer equation (Eq. 1) [53].

$$D_{XRD} = \frac{K\lambda}{\beta \cos\theta} \qquad (1)$$

where K is a constant related to the crystallite shape (K = 0.9), θ is the Bragg angle and β is the contribution of the crystallite size to the full width at half maximum (FWHM) of the corresponding diffraction peak in radians.

The lattice constant a was calculated by using the following relation (Eq. 2):

$$a = d_{hkl}\sqrt{h^2 + k^2 + l^2} \qquad (2)$$

where d the interplanar distance for the plane hkl. The degree of crystallinity (Dx) was calculated using the following formula (Eq. 3) [42]:

$$Crystallinity\ \% = \frac{Diffraction\ peak\ intensity}{Total\ intensity} \times 100 \qquad (3)$$

Paper published in Fuel, Volume 340, 2023, 127523 © 2023 Elsevier Ltd. https://doi.org/10.1016/j.fuel.2023.127523

The crystalline phases were identified by comparison with the Joint Committee on Powder Diffraction Standards (JCPDS) database.

Field Emission Scanning Electron Microscopy (FESEM) (Model: ZEISS Sigma 300) was used to scan the surface morphology of the prepared materials. The particle size was also determined by Transmission Electron Microscopy (TEM) (JEOL, JEM-2100F, 200 kV). The Brunauer-Emmett-Teller (BET) method and Barrett-Joyner-Halenda (BJH) model were used to determine the specific surface area, pore size distribution and pore volumes of the synthesized materials. The magnetization measurements were made under ambient conditions using a vibrating scanning magnetometer (VSM) (Cryogenic Limited PPMS) under an applied field of 1-5 KOe.

2.8. Adsorptive desulfurization experiments

Batch adsorptive desulphurization experiments were conducted by adding specific amount of the prepared magnetic nanoadsorbents with different morphologies to a glass reactor vessel containing 530 ppm sulphur as DBT dissolved in 40 mL *n*-decane as model fuel. The reactor contents were stirred using mechanical stirrer with 300 rpm and 35°C until it reached equilibrium. The nanoadsorbent was separated from the adsorbate by a magnet and the final concentration of DBT in the adsorbate was analyzed for sulphur content using XOS Sindie 7039 XRF Trace Sulphur Fast Batch Testing Fuel Analyzer at the Petroleum Research Centre, Ministry of Oil Iraq. The ADS performance of the nanoadsorbents was evaluated by optimizing experimental parameters like DBT concentration, adsorbent dosage, contact time, and adsorptive temperature. The real oil samples (kerosene and Diesel fuel) were desulfurized applying the optimized set of parameters used in the ADS of the model oil. All the experiments were performed in triplicate and average values were recorded along with the corresponding relative standard deviations. The net adsorption (%) and the adsorption capacity (mg g^{-1}) were calculated using Eqs. (4) and (5), respectively.

$$\%DBT\ Adsorption = \frac{C_i - C_e}{C_i} \times 100 \qquad (4)$$

$$Adsorption\ capacity\ (q_e) = \frac{C_i - C_e}{W} \times V \qquad (5)$$

where C_i and C_e show initial and equilibrium concentration of DBT (mg L^{-1}), V shows the volume of the model oil in litre, and W represents adsorbent dose (g).

3. Results and Discussion

3.1. FTIR, XRD and Raman measurements

The FTIR spectroscopy was used to identify the surface functional groups of the prepared pristine wire-, rod-, and flower-like MnO_2 NPs, their magnetic counterparts (Fig. 2a), and magnetic nanoadsorbents Fe_3O_4@MnO_2-w@AC, Fe_3O_4@MnO_2-r@AC, and Fe_3O_4@MnO_2-f@AC (Fig. 2b).

Paper published in Fuel, Volume 340, 2023, 127523 https://doi.org/10.1016/j.fuel.2023.127523

All of the prepared materials feature distinct bands between 450-650 cm^{-1} related to the vibrations of the manganese-oxygen bond within the manganese dioxide component and the Fe-O bond within the magnetite one. The moderately-intense bands between 1500-1650 cm^{-1} and 1100-1200 cm^{-1} correspond to the bending vibrations of the O-H group (in absorbed water) joined with manganese ions [6]. The more intense broad band around 3100-3408 cm^{-1} is attributable to the O-H stretching vibration of the absorbed water molecules [14, 15]. The presence of water molecules within the NPs might be due to the high surface area of the nano-sized manganese dioxide. FTIR spectra of the prepared magnetic nanoadsorbents presented bands between 1129-1171 cm^{-1}, 1534-1627 cm^{-1} and 3353-3439 cm^{-1} were attributed respectively to the -C-OH (stretching), carboxylic acids, lactonic groups and alcoholic surface functional groups of the activated carbon. The bands in the range of 555-635 cm^{-1} corresponded to the Mn-O and Fe-O stretching vibrations, which confirmed the deposition of magnetic manganese dioxide on the surface of activated carbon.

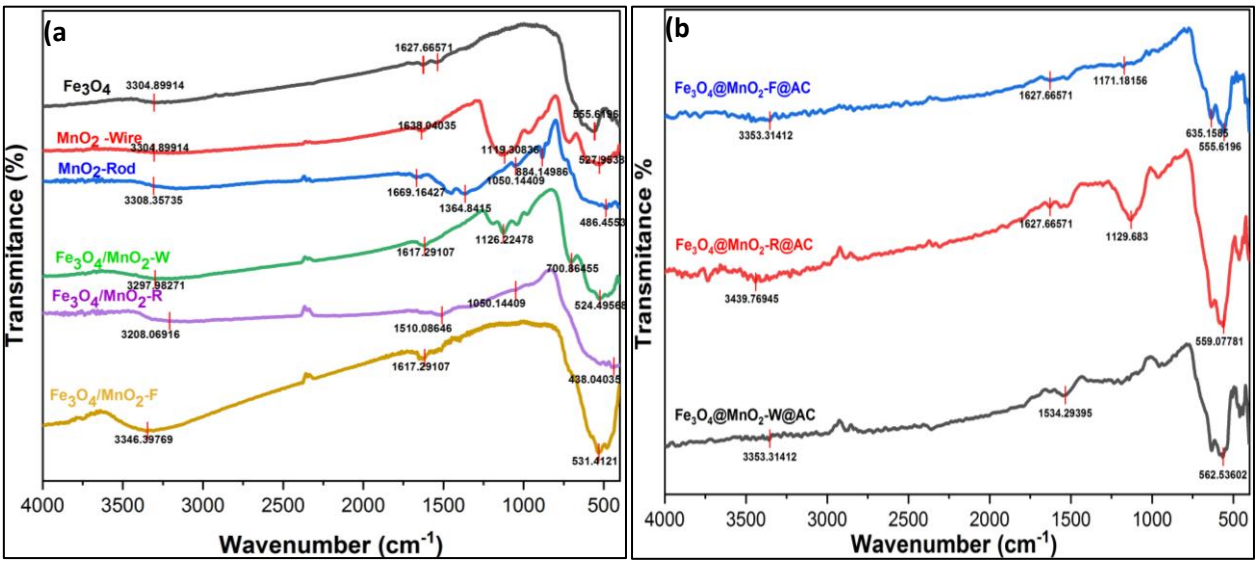

Fig. 2. FTIR spectra of (a) MnO_2 and Fe_3O_4@MnO_2 NPs with different morphologies; (b) Fe_3O_4@MnO_2-w@AC, Fe_3O_4@MnO_2-r@AC, and Fe_3O_4@MnO_2-f@AC magnetic nanoadsorbents.

Powder X-ray diffraction patterns of the prepared materials were measured to find crystalline phases, crystallite sizes and % crystallinity. The prepared wire- and flower-like MnO_2 NPs revealed identical XRD patterns (see Fig. 3a), corresponding to the standard δ-MnO_2 (JCPDS No. 52-0556), which belongs to the birnessite ($K_{0.27}MnO_2.0.54H_2O$) type MnO_2 [51]. The rod-like MnO_2 NPs presented sharp and intense XRD patterns, belonging to the body-centred tetragonal phase (space group 14/m) of the standard α-MnO_2 (JCPDS No. 44-0141) [52]. The sharp and intense peaks in the diffraction pattern of rod-like MnO_2 NPs implied that the α-MnO_2 nanorods had good crystallinity. Unlike using post-treatment at high temperature (500°C) in the study by Wang *et al*. [53], the prepared MnO_2 NPs with different morphologies were not subjected to calcination in this study. However, similar crystal

phase composition but poorer crystallinity was observed in our work. This is attributed to the calcination at high temperature, which could smooth the surface of the adsorbent and improve the crystallinity but reduce the specific surface area. Notably, without calcination at high temperature, birnessite-type MnO_2 was formed for the wire- and flower-like samples, which are different from the results of Wang *et al*.

The crystal phase structures of the prepared Fe_3O_4 NPs as well as wire-, rod-, and flower-like Fe_3O_4@MnO_2 are shown in Fig. 3b. The diffraction peaks located at 30.1°, 35.4°, 39.3°, 43.1°, 53.4°, 57.1°, and 62.5° were respectively attributed to (220), (311), (222), (400), (422), (511), and (440) crystal planes of the cubic inverse spinel Fe_3O_4 NPs. The XRD pattern showed good consistency with that of pure Fe_3O_4 (JCDPS 85-1436) [54]. The XRD patterns for wire-, rod-, and flower-like Fe_3O_4@MnO_2 exhibited the same crystalline phase with poorer crystallinity as for the pure α- and δ-MnO_2 NPs, with the existence of diffraction peaks of pristine Fe_3O_4. The newly-synthesized Fe_3O_4@MnO_2-w@AC, Fe_3O_4@MnO_2-r@AC, and Fe_3O_4@MnO_2-f@AC magnetic nanoadsorbents featured new XRD diffraction peaks at 23° and 43° (see Fig. 3c) belonging to (002) and (100) crystal planes of coherent and parallel stacked graphitic sheets (Graphite PDF 26-1079) of the annealed activated carbon [55].

Raman spectroscopy is a powerful technique for determination of the structural defects in the crystal structure of our magnetic manganese dioxide-decorated activated carbon. The Raman spectra of Fe_3O_4@MnO_2-w@AC, Fe_3O_4@MnO_2-r@AC, and Fe_3O_4@MnO_2-f@AC magnetic nanoadsorbents (Fig. 3d) feature two characteristic bands, respectively denoted as the D-band and G-band, belonging to annealed activated carbon. The D band at 1345 cm^{-1} is due to the disordered graphite structure which relates to defects of the graphitic regions that exist in annealed activated carbon derived from palm kernel shell. The G band at 1593 cm^{-1} indicates the presence of sp^2 carbon network structure which is composed of either C=C chains or aromatic ring structures [55]. In addition, the Raman spectrum presented peaks at 280, 410, 510, 580 and 620 cm^{-1} belonging to vibrational modes of Mn-O bonds of α and δ MnO_2 NPs [56]. The typical vibrational modes assigned to magnetite (Fe_3O_4) are situated at 670 cm^{-1} correlate to the A_1g mode; 538 and 306 cm^{-1} correspond to the T_2g mode of Fe-O bonds of Fe_3O_4 NPs [57]. Moreover, the measured I_D/I_G values of 0.768, 1.015, and 0.868, for Fe_3O_4@MnO_2-f@AC, Fe_3O_4@MnO_2-r@AC, and Fe_3O_4@MnO_2-w@AC, respectively showed that the annealed activated carbons retained their graphitic character after decoration with different forms of magnetic manganese dioxide.

3.2. Surface studies and elemental compositions of the prepared materials

Surface morphologies of the hydrothermally prepared pristine MnO_2 NPs and magnetic nanoadsorbents were investigated by FESEM and TEM techniques, while the elemental

compositions were determined by EDAX elemental mapping spectroscopy. The EDAX elemental mapping results (see Fig. 4a-c) for the prepared Fe_3O_4@MnO_2-w@AC, Fe_3O_4@MnO_2-w@AC, and Fe_3O_4@MnO_2-w@AC magnetic nanoadsorbents indicated a good dispersion of Fe, O, and Mn elements over activated carbon and the larger amount of Mn element was observed in the magnetic nanoadsorbent with wire-like morphology (Fig. 4a).

Fig. 5a-f illustrates the FESEM micrographs and TEM images of the pristine MnO_2 and magnetic MnO_2 NPs with different morphologies. The MnO_2 NPs with different morphologies (Fig. 5a,c,e) and their magnetic counterparts (Fig. 5b,d,f) were easily distinguished by their distinctive shapes. The FESEM micrograph of δ-MnO_2 nanowire (Fig. 5a) revealed long and crossed nanowires (28.04 nm wire diameter), while the TEM image of magnetic δ-MnO_2 nanowire (Fig. 5b) confirmed the coating of single wire-like MnO_2 with Fe_3O_4 NPs. The FESEM micrograph (Fig. 5c) showed a smooth and uniform structure for α-MnO_2 nanorods with average length and diameter of about 180 nm and 25 nm, respectively. The TEM images (Fig. 5d) for magnetic α-MnO_2 nanorods clearly displayed a uniform coating of single rod-like MnO_2 by Fe_3O_4 NPs. For flower-like δ-MnO_2, FESEM (Fig. 5e) revealed spherical shape (370-500 nm flowers estimated size) featuring flower petals interleaved with thin nanoplates (thickness 8-10 nm and length 37-45 nm), each of which appeared to grow perpendicularly from the inner core [58]. The TEM analysis (Fig. 5f) for magnetic δ-MnO_2 nanoflowers indicates a typical hierarchical structure of flower-like MnO_2 coated with Fe_3O_4 NPs. The FESEM micrographs of the hydrothermally synthesized magnetic nanoabsorbents Fe_3O_4@MnO_2-w@AC, Fe_3O_4@MnO_2-r@AC, and Fe_3O_4@MnO_2-f@AC are presented in Fig. 6a-f. The FESEM micrograph of undecorated activated carbon (Fig. 5a) showed a rough surface of graphitic carbon sheets, while the wire- and rod-like magnetic MnO_2 decorated with activated carbon i.e. Fe_3O_4@MnO_2-w@AC and Fe_3O_4@MnO_2-r@AC (Fig. 5b,e,f) displayed numerous well-distributed wires and rods on the surface of activated carbon. Homogeneously and densely attached flower-like magnetic MnO_2 NPs on the surface of activated carbon were observed in the FESEM micrographs (Fig. 5c and d) for Fe_3O_4@MnO_2-f@AC magnetic nanoadsorbent.

Table 1. Physical parameters of the prepared wire-, rod-, and flower-like magnetic MnO_2 NPs.

Parameters	**Fe_3O_4@MnO_2-w**	**Fe_3O_4@MnO_2-r**	**Fe_3O_4@MnO_2-f**
Crystallite size (D_{SEM}) nm	28.83	40.04	34.85
Crystallite size (D_{TEM}) nm	27.33	43.8	34.08
Average crystallite size (D_{XRD}) nm	8.735	34.343	22.653
Specific surface area (S_{BET}) $m^2\ g^{-1}$	96	100	112
Pore volume (V_p) $cm^3\ g^{-1}$	0.3850	0.2006	0.3519
Mean pore diameter (D_p) nm	8.26	2.80	5.88
Saturation magnetization (M_S) emu g^{-1}	21.87	24.15	20.46
Remanence (M_R) emu g^{-1}	1.45	3.90	3.460
Coercive field (H_C) KO_e	1.008	0.712	0.58

Authors' Accepted Manuscript
Paper published in Fuel, Volume 340, 2023, 127523 © 2023 Elsevier Ltd. https://doi.org/10.1016/j.fuel.2023.127523

Table 2. Physical parameters of the prepared Fe_3O_4@MnO_2@AC with different morphologies.

Parameters	AC	Fe_3O_4@MnO_2-w@AC	Fe_3O_4@MnO_2-r@AC	Fe_3O_4@MnO_2-f@AC
S_{BET} m^2 g^{-1}	596	480	312	340
V_p cm^3 g^{-1}	0.1248	0.3526	0.2010	0.3338
D_p nm	2.214	10.5	3.35	4.26
M_S emu g^{-1}		18.37	21.50	17.35
M_R emu g^{-1}		1.950	3.150	2.552
H_C KOe		0.020	0.0223	0.0220

S_{BET}: Specific surface area**; M_S:** Saturation magnetization**; V_p:** pore volume**; M_R:** Remanence**; H_C:** Coercive field**; AC:** Activated carbon**; D_p:** pore diameter

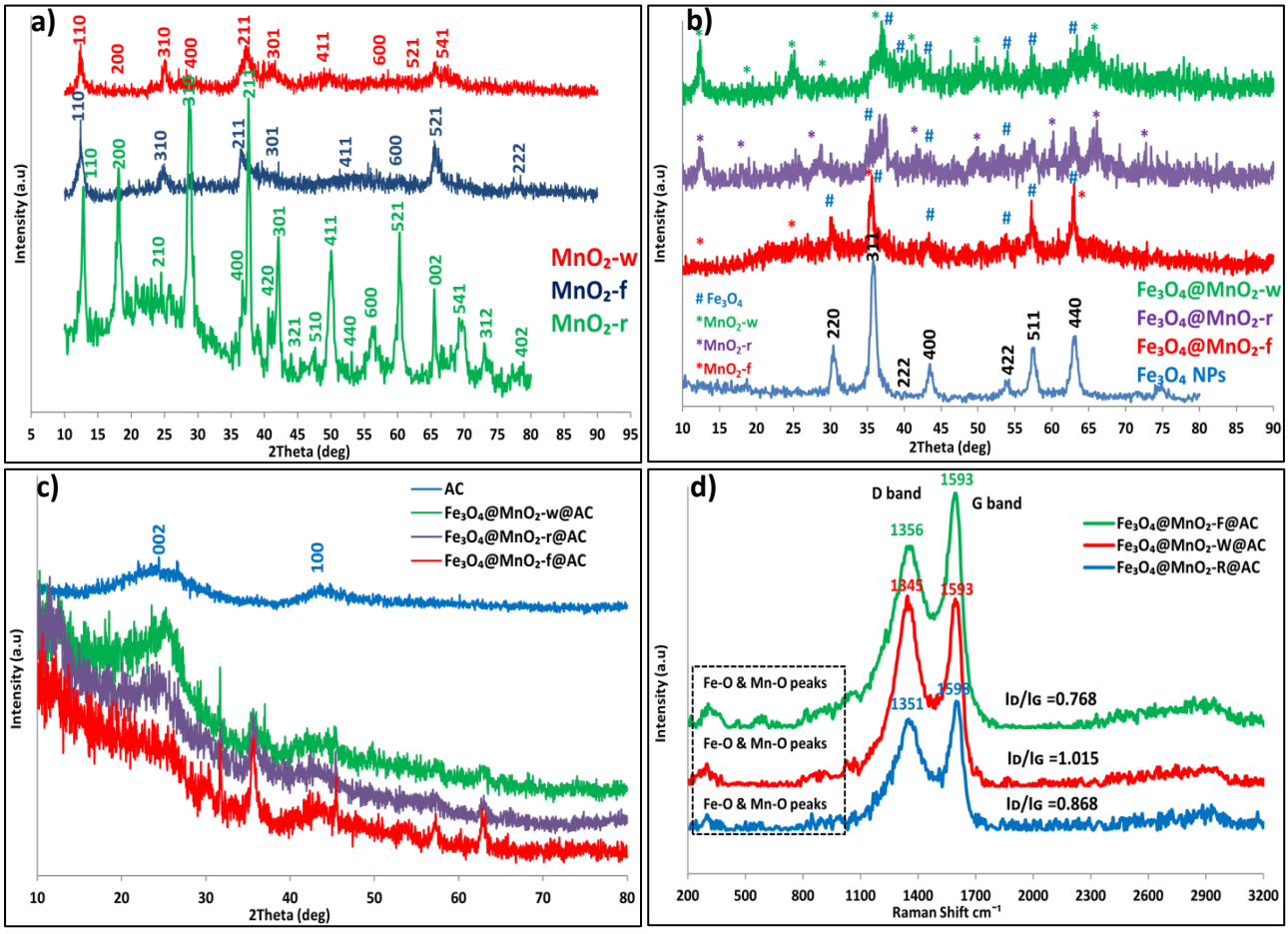

Fig. 3. XRD patterns: (a) pristine wire-, rod-, and flower-like MnO_2 NPs, (b) wire-, rod-, and flower-like magnetic MnO_2, (c) wire-, rod-, and flower-like magnetic MnO_2 decorated activated carbon, and (d) Raman shifts for the prepared magnetic nanoadsorbents.

Paper published in Fuel, Volume 340, 2023, 127523 https://doi.org/10.1016/j.fuel.2023.127523

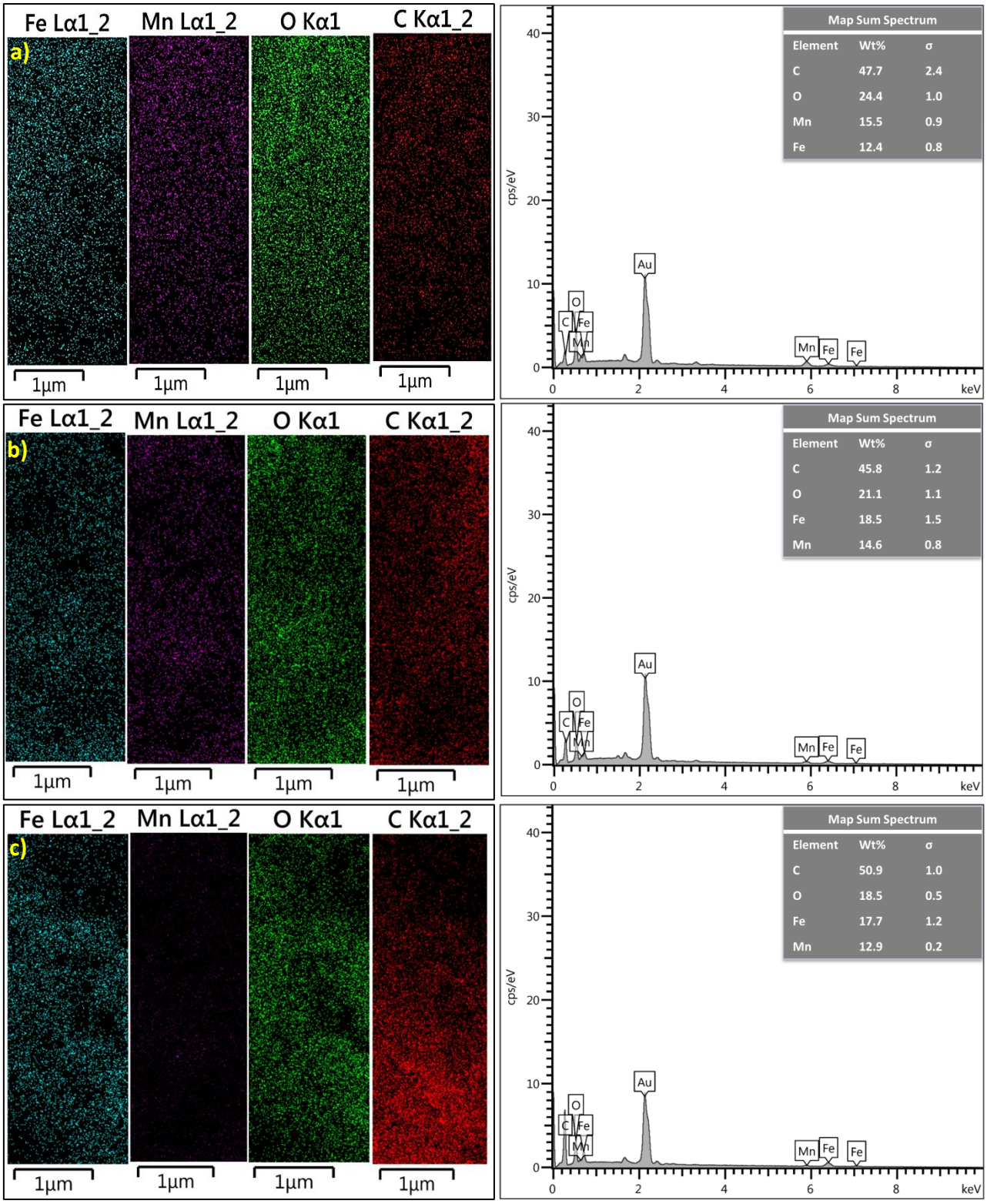

Fig. 4. EDAX elemental mapping images of (a) Fe_3O_4@MnO_2-w@AC, (b) Fe_3O_4@MnO_2-r@AC, and (c) Fe_3O_4@MnO_2-f@AC magnetic nanoadsorbents.

Paper published in Fuel, Volume 340, 2023, 127523 https://doi.org/10.1016/j.fuel.2023.127523

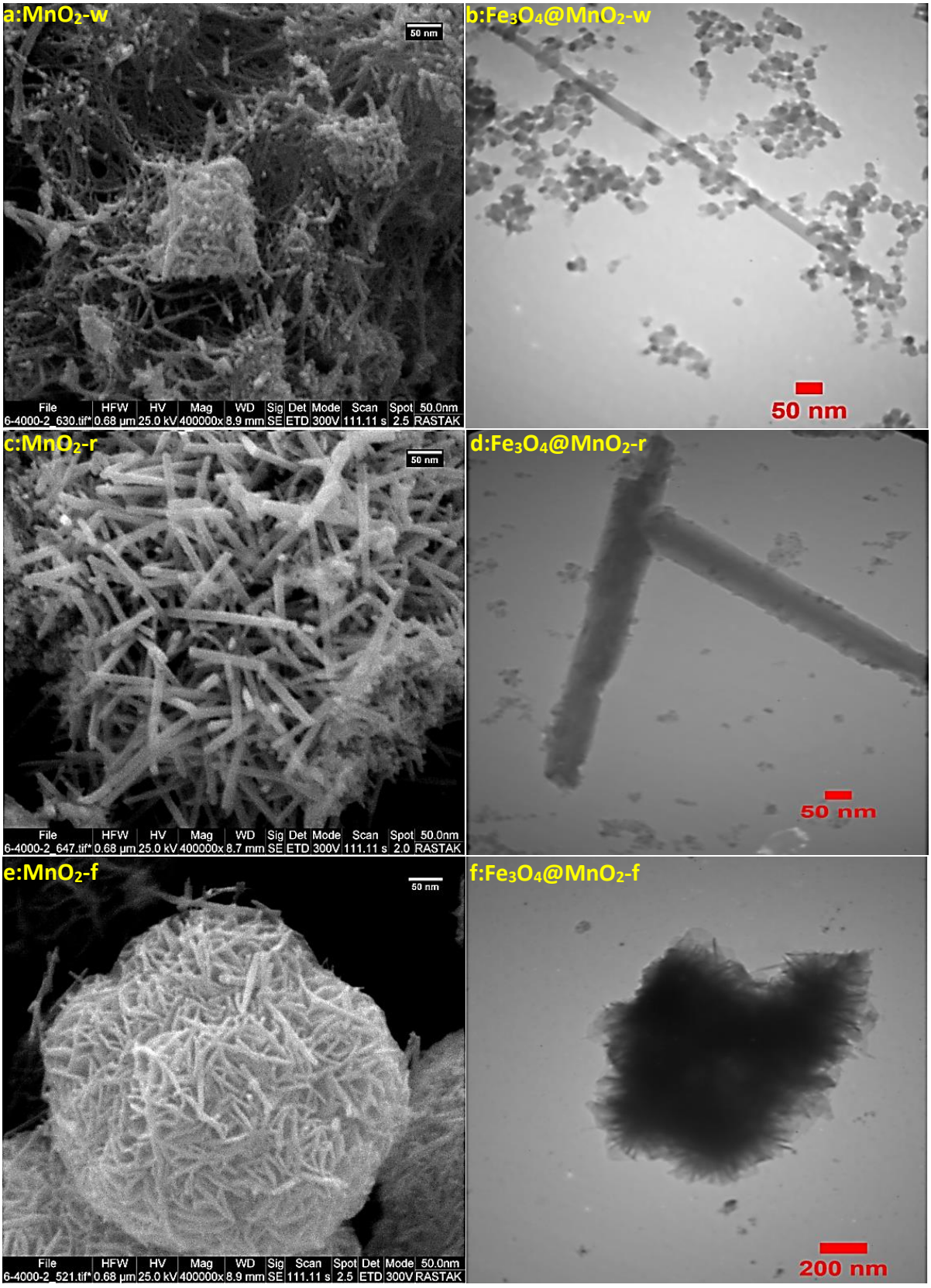

Fig. 5. FESEM micrographs: (a) MnO_2-w NPs, (c) MnO_2-r NPs, and (e) MnO_2-f NPs; TEM images: (b) Fe_3O_4@MnO_2-w, (d) Fe_3O_4@MnO_2-r, and (f) Fe_3O_4@MnO_2-f magnetic NPs.

Paper published in Fuel, Volume 340, 2023, 127523 https://doi.org/10.1016/j.fuel.2023.127523

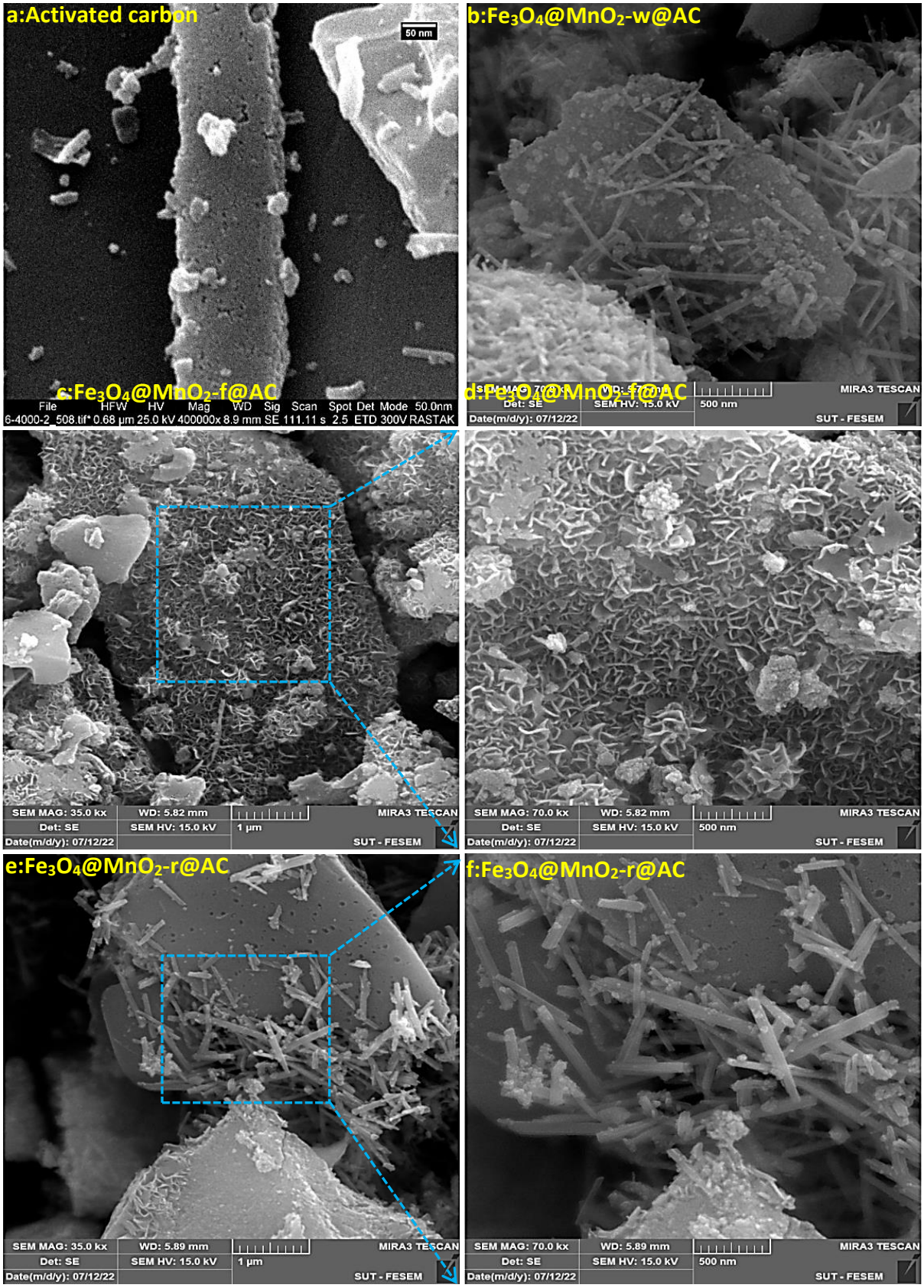

Fig. 6. FESEM micrographs: (a) undecorated activited carbon, (b) Fe_3O_4@MnO_2-w@AC, (c) and (d) Fe_3O_4@MnO_2-f@AC, (e) and (f) Fe_3O_4@MnO_2-r@AC magnetic nanoadsorbents with different magnifications.

Paper published in Fuel, Volume 340, 2023, 127523 © 2023 Elsevier Ltd. https://doi.org/10.1016/j.fuel.2023.127523

3.3. BET analysis

Brunauer-Emmett-Teller (BET) method was used to find the specific surface area S_{BET}, while the pore volume Vp and pore size Dp of the magnetic nanoadsorbents were determined *via* the Barrett-Joyner-Halenda (BJH) model. The N_2 adsorption-desorption isotherms and pore size distribution curves of the various nanomaterials are shown in Fig. 7a-i. According to the IUPAC classification, all the wire-, rod-, and flower-like magnetic MnO_2 NPs exhibited type IV isotherms with a typical H_3 type hysteresis loop (see Fig. 7a,b,c) occur between (P/P_o= 0.3-0.99), indicating mono and multilayers adsorption over a mesoporous solid [54, 59]. The calculated S_{BET} values (see Table 1) for the wire-, rod- and flower-like magnetic MnO_2 NPs were 96, 100 and 112 $m^2\ g^{-1}$, respectively. The values of the pore volume and mean pore diameter were 0.3850, 0.2006, and 0.3519 $cm^3\ g^{-1}$ and 8.26, 2.80, and 5.88 nm, respectively (see Fig. 7d). The N_2 adsorption-desorption isotherms and pore size distribution curves of the activated carbon produced from palm kernel shell as well as the newly-synthesized Fe_3O_4@MnO_2-w@AC, Fe_3O_4@MnO_2-r@AC, and Fe_3O_4@MnO_2-f@AC magnetic nanoadsorbents are shown in Fig 7e-i. The N_2 adsorption-desorption isotherm (see Fig. 7e) of undecorated AC revealed a type I & IV isotherm with an H_4 hysteresis loop at relatively low pressure P/P_o and high N_2 adsorption capacity (435 $cm^3\ g^{-1}$) indicating a micro-mesoporous structure with pore diameters between 1.22-2.214 nm, total pore volume of 0.1248 $cm^3\ g^{-1}$ and S_{BET} of 596 $m^2\ g^{-1}$. Whereas the newly-synthesized Fe_3O_4@MnO_2-w@AC, Fe_3O_4@MnO_2-r@AC and Fe_3O_4@MnO_2-f@AC magnetic nanoadsorbents revealed type IV isotherms with H_3 type hysteresis loops (see Fig. 7f-h) at relatively high pressure P/P_o, and N_2 adsorption capacities of 293, 254 and 240 $cm^3\ g^{-1}$, respectively. The calculated S_{BET} values (see Table 2) were 480 $m^2\ g^{-1}$ for Fe_3O_4@MnO_2-w@AC, 312 $m^2\ g^{-1}$ for Fe_3O_4@MnO_2-r@AC, and 340 $m^2\ g^{-1}$ for Fe_3O_4@MnO_2-f@AC, while the pore volume and pore size values (see Fig. 7i) were 0.3526 $cm^3\ g^{-1}$ and 10.5 nm, 0.2010 $cm^3\ g^{-1}$ and 3.35 nm, and 0.3338 $cm^3\ g^{-1}$ and 4.26 nm, respectively. However, these new textural properties may be due to partial hydrothermal anchoring of magnetic MnO_2 of different morphologies over activated carbon surface. Thus the designed nanopores of our novel Fe_3O_4@MnO_2-w@AC, Fe_3O_4@MnO_2-r@AC, and Fe_3O_4@MnO_2-f@AC magnetic nanoadsorbents are expected to facilitates the sulphur adsorption from commercial fuel due to high specific surface area and sufficient volume adsorbed.

Authors' Accepted Manuscript
Paper published in Fuel, Volume 340, 2023, 127523 https://doi.org/10.1016/j.fuel.2023.127523

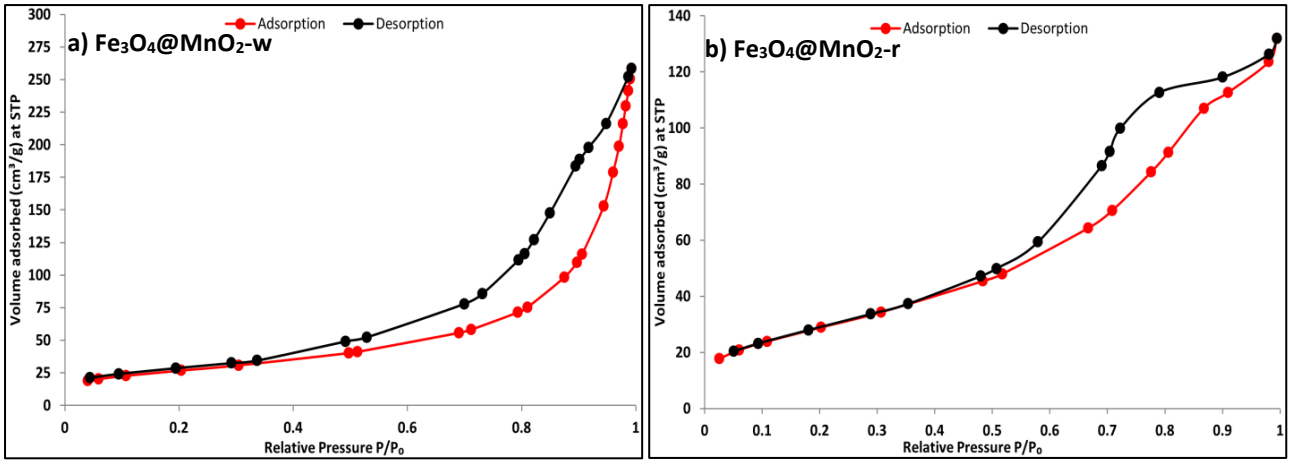

1

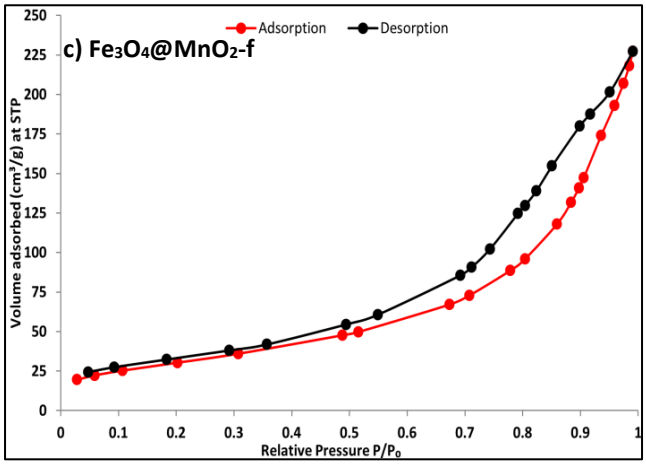

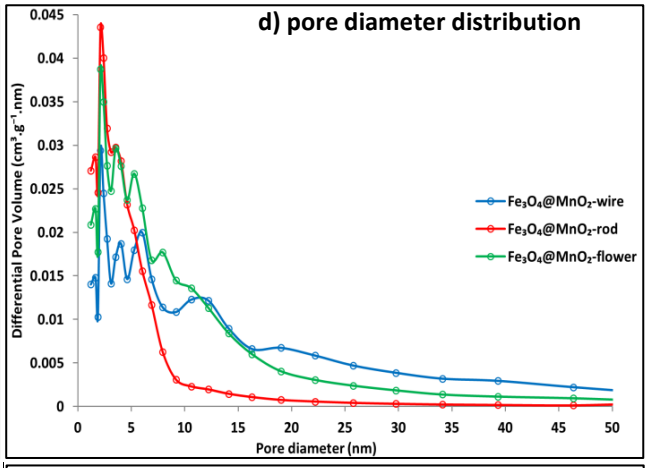

2

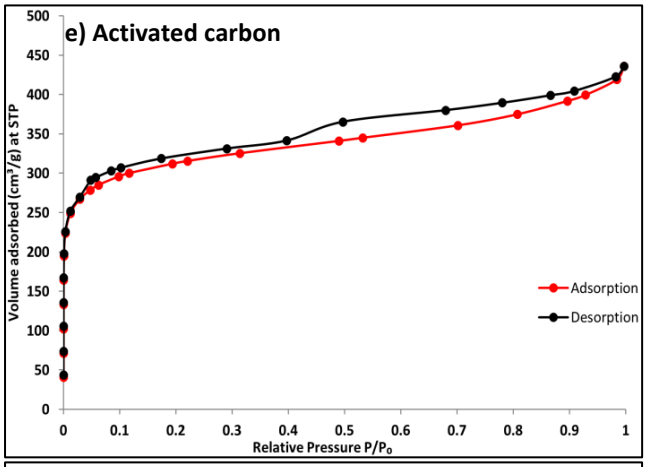

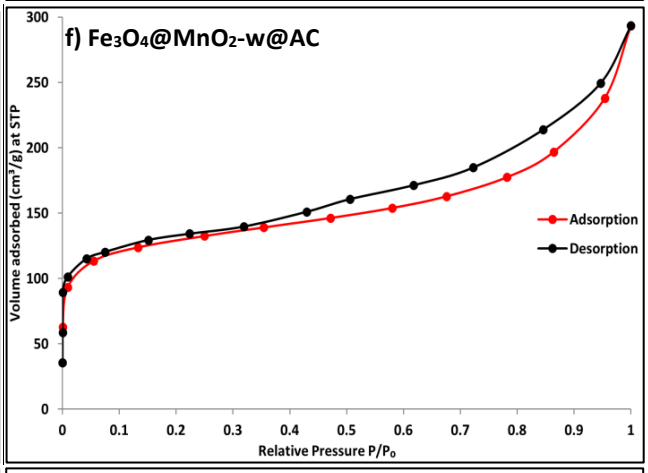

3

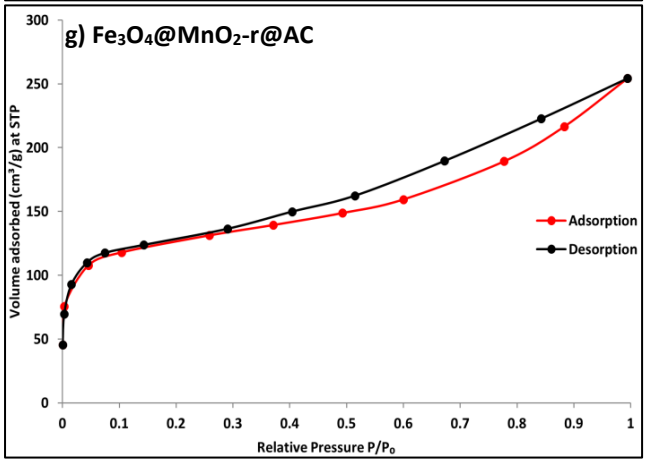

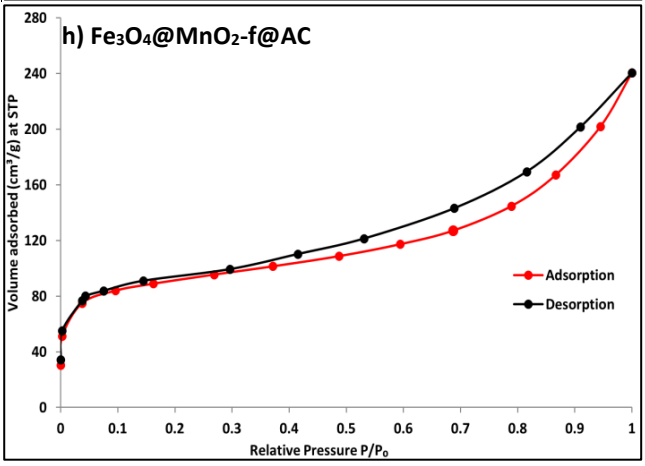

4

Paper published in Fuel, Volume 340, 2023, 127523 https://doi.org/10.1016/j.fuel.2023.127523

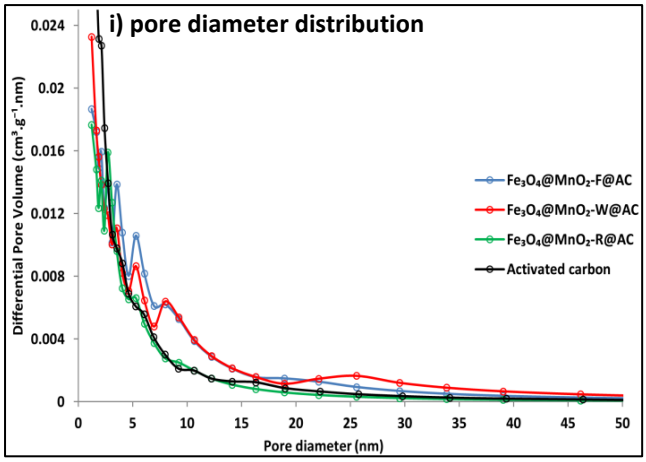

Fig. 7. N_2 adsorption-desorption isotherms: (a) Fe_3O_4@MnO_2-w NPs, (b) Fe_3O_4@MnO_2-r NPs, (c) Fe_3O_4@MnO_2-f NPs, (e) activated carbon, (f) Fe_3O_4@MnO_2-w@AC, (g) Fe_3O_4@MnO_2-r@AC, and (h) Fe_3O_4@MnO_2-f@AC; the corresponding diameter distribution plots are labelled (d) and (i), respectively.

3.3. VSM measurements

In this work, Fe_3O_4 NPs were incorporated with different morphologies of MnO_2 NPs in order to ensure the recyclability of our newly-synthesized nanoadsorbents. Therefore, the magnetic hysteresis loops were analyzed by a vibrating sample magnetometer (VSM) at room temperature; the results are shown in Fig 8 and the collected magnetic parameters are listed in Table 1. For the magnetic MnO_2 NPs with different morphologies, the saturation magnetization Ms was still very high after Fe_3O_4 NPs incorporation (see Figs. S1b and S2 in supporting information file). The Ms value for Fe_3O_4 NPs was 63.56 emu g^{-1}, while the values for wire-, rod- and flower-like Fe_3O_4@MnO_2 NPs were 21.87, 24.15 and 20.46 emu g^{-1}, respectively. The VSM magnetization curves (see Fig. 8) of our newly-synthesized Fe_3O_4@MnO_2-w@AC, Fe_3O_4@MnO_2-r@AC and Fe_3O_4@MnO_2-f@AC magnetic nanoadsorbents confirmed soft superparamagnetic properties with minimal remanence Mr and coercivity Hc (see Table 2), with saturation magnetization Ms values of 18.37, 21.50 and 17.35 emu g^{-1}, respectively. The reduction in the saturation magnetization of the prepared magnetic nanoadsorbents may be attributed to the diamagnetic feature of activated carbon and/or the presence of a magnetically dead or antiferromagnetic layer on the surface of the activated carbon [60]. However, it has been reported that a minimum saturation magnetization of 16.3 emu g^{-1} is required for effective magnetic separation, thus our prepared magnetic nanoadsorbents with saturation magnetization higher than this threshold should be useable for magnetic separation from an aqueous mixture when an external magnetic field is applied [61].

Paper published in Fuel, Volume 340, 2023, 127523 https://doi.org/10.1016/j.fuel.2023.127523

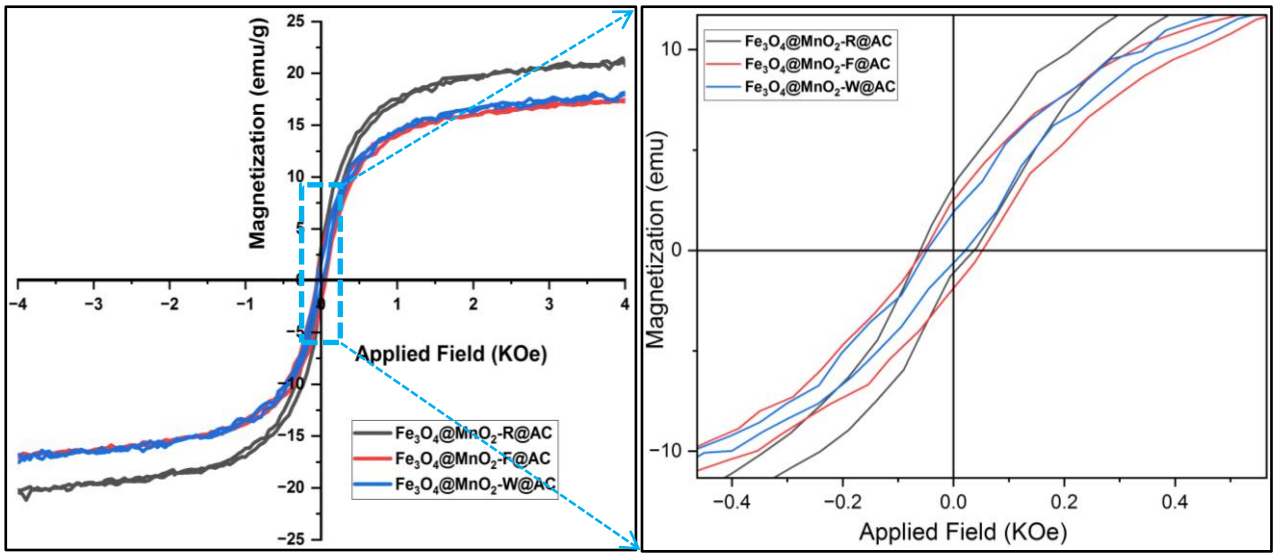

Fig. 8. VSM magnetization curves of the prepared magnetic nanoadsorbents.

3.4. Adsorptive desulphurization performance of the prepared magnetic nanoadsorbents

To investigate the effectiveness of the prepared Fe_3O_4@MnO_2-w@AC, Fe_3O_4@MnO_2-r@AC and Fe_3O_4@MnO_2-f@AC magnetic nanoadsorbents in the ADS of liquid fuels, a range of concentrations of DBT dissolved in n-decane as model fuel were used. The ADS performance of the prepared wire-, rod-, and flower-like magnetic MnO_2 NPs before anchoring on activated carbon was first evaluated. However, ADS process conditions such as temperature, DBT concentration, adsorbent dose and contact time were studied in detail. Fig. S3 shows the effect of using different doses (0.1-0.4 g per 40 mL; i.e. 1-10 g L^{-1}) of Fe_3O_4@MnO_2-w magnetic NPs on the sulphur removal from model fuel containing 1330 ppm sulphur as DBT, at 35°C adsorption temperature and 100 min contact time. The sulphur removal efficiency remarkably increased from 25.6% to 60.9% as the dose increased from 0.1 to 0.4 g. Therefore 0.4 g per 40 mL was considered as an appropriate adsorbent dosage to complete the study.

Different DBT concentrations (530, 830, and 1330 ppm) were used to study the ADS performance of the prepared Fe_3O_4@MnO_2-w, Fe_3O_4@MnO_2-r, and Fe_3O_4@MnO_2-f magnetic NPs at 35°C, 100 min contact time and 0.4 g adsorbent dose. The ADS results showed a noticeable decline in sulphur removal efficiency upon using 830 and 1330 ppm DBT concentrations (see Fig. S4, S5, and Fig. 9a). This decline might be explained by the fact that as DBT concentration increased, the driving force for the diffusion of DBT molecules into the adsorbent pores increased [5]. Consequently, saturation of the adsorbent active sites by adsorbed DBT became faster, which might account for the reduction in DBT adsorption with concentration. Thus, 530 ppm was considered as the optimal DBT concentration in the next experiments. The calculated sulphur removal efficiencies using 530 ppm DBT concentration, 0.4 g adsorbent dose, 35°C adsorption temperature and 100 min contact time

were 81.16% for Fe_3O_4@MnO_2-w, 68.7% for Fe_3O_4@MnO_2-r and 41.6% for Fe_3O_4@MnO_2-f (see Fig. 9b).

Different temperatures (25, 35, 45 and 60°C) in the ADS of a model fuel containing 530 ppm sulphur content as DBT; 0.4 g adsorbent dose and 100 min contact time were used. The results revealed a slight increase in the sulphur removal from 79.21 to 81.16% for Fe_3O_4@MnO_2-w, from 66.47 to 68.73% for Fe_3O_4@MnO_2-r, and from 39.93 to 41.61% for Fe_3O_4@MnO_2-f upon temperature increase from 25 to 35°C (see Fig. 10a). At elevated temperatures (45 and 60°C), an obvious decrease in the sulphur removal efficiency was observed. The reduction in the DBT adsorption above 35°C may correlate with the increasing molecular kinetic energy, in turn weakening the attractive interactions between DBT molecules and the adsorbent active sites. Therefore, 35°C adsorption temperature, 530 ppm DBT concentration and 0.4 g adsorbent dose were chosen as the ADS process conditions to be implemented in the upcoming experiments.

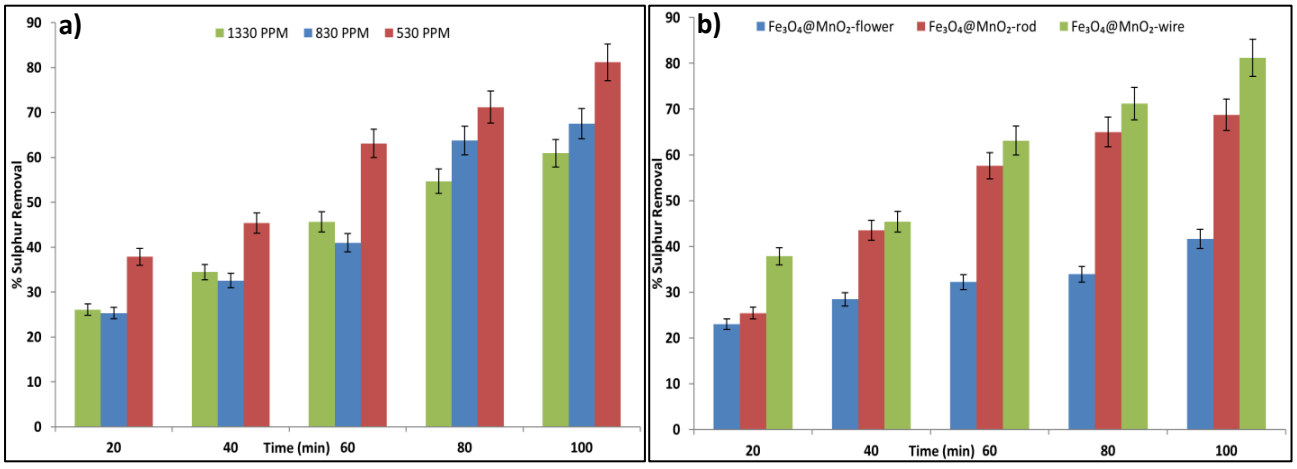

Fig. 9. Sulphur removal efficiency: (a) Fe_3O_4@MnO_2-w using model fuels with different DBT concentration; (b) Fe_3O_4@MnO_2-w, Fe_3O_4@MnO_2-r, and Fe_3O_4@MnO_2-f using model fuel with 530 ppm DBT concentration. ADS conditions: 0.4 g adsorbent dose, 35°C adsorption temperature, and 100 min contact time.

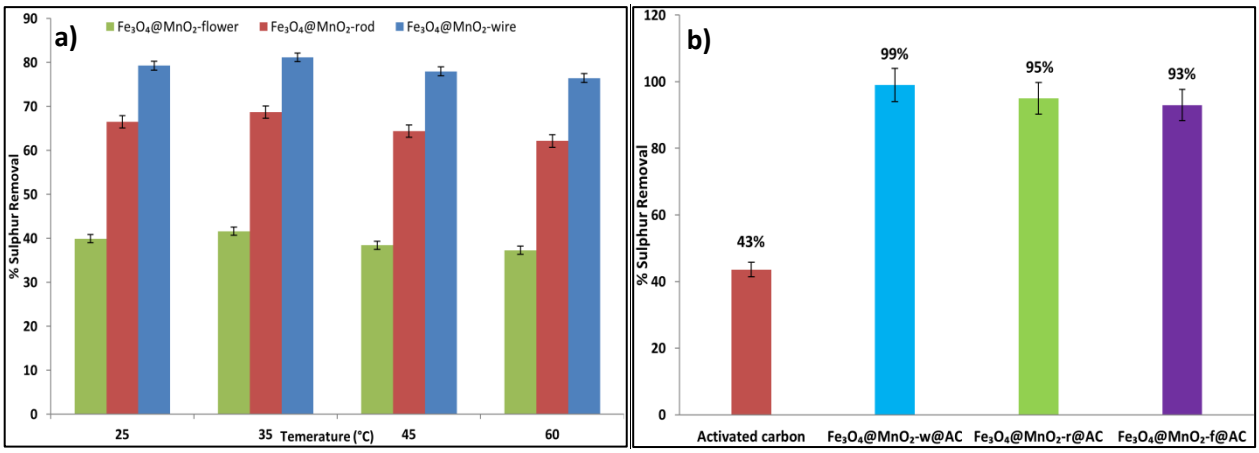

Paper published in Fuel, Volume 340, 2023, 127523 © 2023 Elsevier Ltd. https://doi.org/10.1016/j.fuel.2023.127523

Fig. 10. Sulphur removal efficiency: (a) Fe_3O_4@MnO_2-w, Fe_3O_4@MnO_2-r, and Fe_3O_4@MnO_2-f using model fuel with 530 ppm DBT, 0.4 g adsorbent dose, 100 contact time and different adsorption temperatures; (b) Activated carbon AC, Fe_3O_4@MnO_2-w@AC, Fe_3O_4@MnO_2-r@AC and Fe_3O_4@MnO_2-f@AC using model fuel with 530 ppm DBT, 0.4 g adsorbent dose, 35°C, and 100 min contact time.

The Fe_3O_4@MnO_2-w@AC, Fe_3O_4@MnO_2-r@AC, and Fe_3O_4@MnO_2-f@AC magnetic nanoadsorbents were utilized in the ADS of n-decane containing 530 ppm DBT as model fuel under optimized ADS process conditions. Undecorated activated carbon made from palm kernel shells was also tested for comparison. The graphical results (see Fig. 10b) indicated poor ADS performance (43% sulphur removal) by undecorated AC, while the sulphur removal efficiencies were 99%, 95%, and 93% for Fe_3O_4@MnO_2-w@AC, Fe_3O_4@MnO_2-r@AC and Fe_3O_4@MnO_2-f@AC magnetic nanoadsorbents, respectively.

However, the novel magnetic nanoadsorbents showed promising ADS performance using DBT in n-decane as model fuel, but its industrial potential could not be assessed until its possible use in commercial fuel was investigated. Therefore, kerosene with 430 ppm and diesel fuel with 1050 ppm total sulphur content supplied by North Refineries Company were used as commercial fuels. The parent wire-, rod-, and flower-like magnetic MnO_2 NPs were first tested using the optimized ADS conditions i.e. 35°C adsorptive temperature, 0.4 g adsorbent dose per 40 mL of real fuel, and 100 min contact time. The results displayed in Fig. 11a reveal weak sulphur uptakes by Fe_3O_4@MnO_2-w, Fe_3O_4@MnO_2-r, and Fe_3O_4@MnO_2-f using kerosene and diesel fuel. The undecorated activated carbon shows poor ADS performance 33.64% with kerosene and 18.38% sulphur removal with diesel fuel. Whereas, our new Fe_3O_4@MnO_2-w@AC, Fe_3O_4@MnO_2-r@AC, and Fe_3O_4@MnO_2-f@AC magnetic nanoadsorbents exhibited excellent sulphur removal efficiencies, i.e. 97.6%, 93%, and 91.6%, respectively when commercial kerosene fuel (430 ppm sulphur content) was used (see Fig. 11b). On the other hand, when commercial diesel fuel (1050 ppm sulphur content) was used, the sulphur removal efficiencies were 51.6% for Fe_3O_4@MnO_2-w@AC, 43.5% for Fe_3O_4@MnO_2-r@AC, and 33% for Fe_3O_4@MnO_2-f@AC in optimum conditions (see Fig. 12a). The existence of more complex aromatic sulphur compounds, such as benzothiophene, dibenzothiophene, 4-methyl dibenzothiophene, 2,4-dimethyl dibenzothiophene, 4,6-dimethyl dibenzothiophene, 2-dimethyl dibenzothiophene, and 2,4,6-trimethyl dibenzothiophene in diesel oil may increase the steric hindrance due to the alkyl side-chains, resulting in an overall reduction in ADS efficiency. Nonetheless, it was noted that higher doses of the new magnetic nanoadsorbents resulted in an improvement in ADS from 51.5% to 90% sulphur recovery for Fe_3O_4@MnO_2-w@AC, from 43.5%

Paper published in Fuel, Volume 340, 2023, 127523 © 2023 Elsevier Ltd. https://doi.org/10.1016/j.fuel.2023.127523

to 83.6% for Fe_3O_4@MnO_2-r@AC and from 33% to 75% for Fe_3O_4@MnO_2-f@AC when the adsorbent doses increased from 0.4 to 0.8 g per 40 mL of tested diesel fuel (see Fig. 12b).

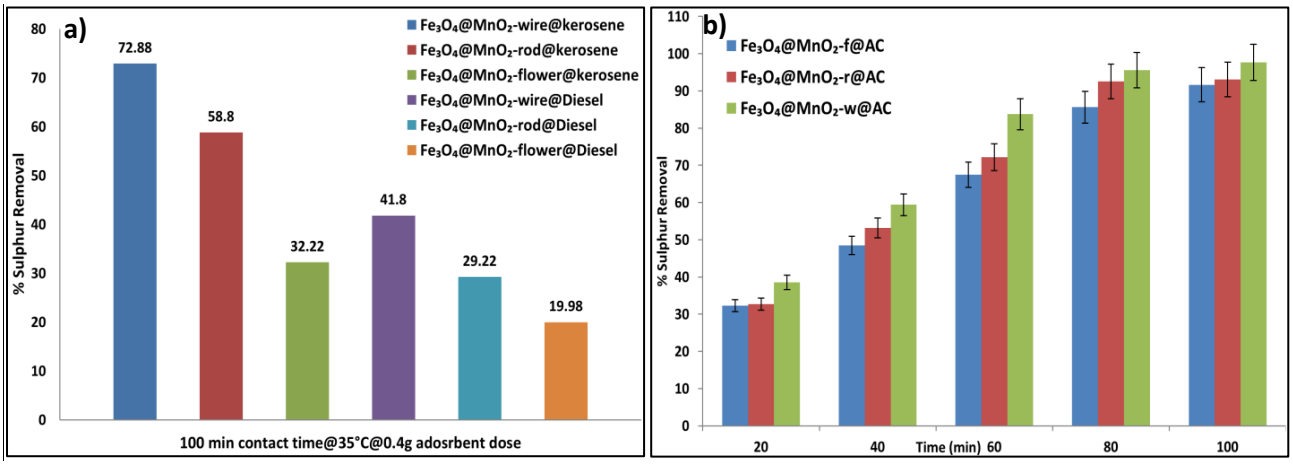

Fig. 11. Sulphur removal efficiencies: (a) Fe_3O_4@MnO_2-w, Fe_3O_4@MnO_2-r and Fe_3O_4@MnO_2-f using commercial kerosene and diesel fuel with 430 ppm and 1050 ppm total sulphur content; (b) Fe_3O_4@MnO_2-w@AC, Fe_3O_4@MnO_2-r@AC and Fe_3O_4@MnO_2-f@AC using commercial kerosene fuel. ADS conditions: 0.4 g adsorbent dose, 35°C adsorption temperature and 100 min contact time.

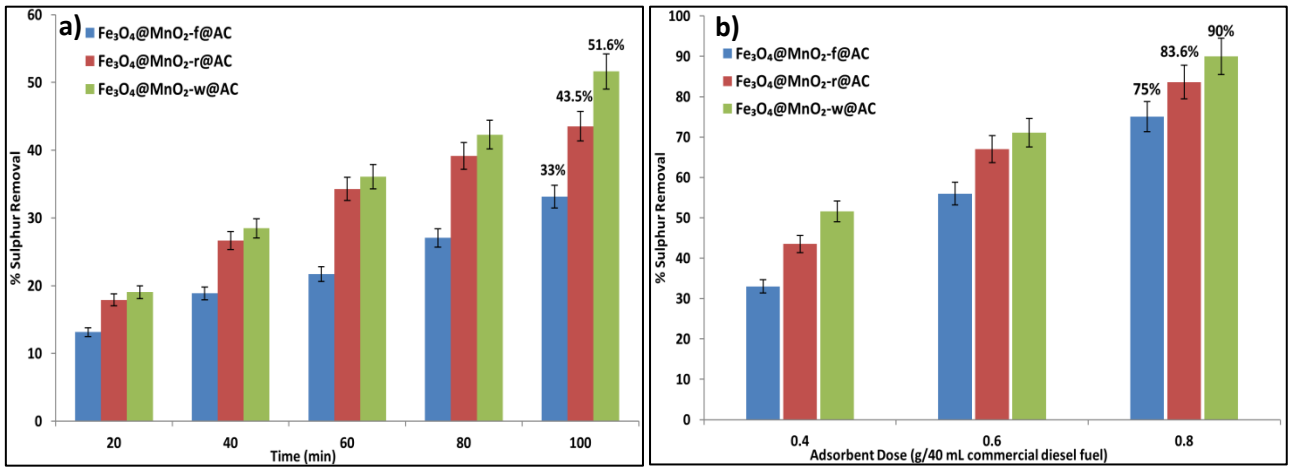

Fig. 12. Sulphur removal efficiency: (a) Fe_3O_4@MnO_2-w@AC, Fe_3O_4@MnO_2-r@AC, and Fe_3O_4@MnO_2-f@AC using commercial diesel fuel (1050 ppm sulphur content); (b) Fe_3O_4@MnO_2-w@AC, Fe_3O_4@MnO_2-r@AC, and Fe_3O_4@MnO_2-f@AC using commercial diesel fuel (1050 ppm sulphur content) and different adsorbent doses at 35°C adsorption temperature and 100 min contact time.

The effectiveness of the studied magnetic nanoadsorbents in ADS of organic sulphur was compared to those described in similar studies. Table 3 shows the ADS's optimum conditions for sulphur removal over various adsorbents as well as the newly-designed magnetic nanoadsorbents utilized in this work.

Table 3: Selected adsorbents for removal of sulphur from model and diesel fuels.

Adsorbent	S. content (ppm)	Time (min)	Temp. (°C)	Dose (g)	Sulphur removal	Ref.
MnO@AC	50 as DBT	90	25	0.05	80%	[62]
ASS	Diesel: 1390	100	35	18	33%	[63]
Zn-AC	200 as DBT	120	30	0.15	95.7%	[5]
CoCu-AC	Model diesel: 50	100	25	0.25	87%	[64]
FeO-Z	2700 as SO_2	28.5	25	100	80.3%	[65]
MnO_2-CeO_2	1000 as SO_2	300	400	0.15	0.289 g g^{-1}	[7]
MnO_2-NaY	1000 as SO_2	300	400	0.15	0.209 g g^{-1}	[7]
Fe_3O_4@MnO_2-w@AC Fe_3O_4@MnO_2-r@AC Fe_3O_4@MnO_2-f@AC	530 as DBT	100	35	0.4	99% 95% 93%	This work
AC: activated carbon, ASS: activated sewage sludge FeO-Z: modified zeolite with iron oxide nanoparticles						

3.5. Adsorption kinetics and evaluation

To gain knowledge of the ADS performance of our magnetic nanoadsorbents, the adsorption kinetics were investigated by employing the pseudo first-order [66], pseudo second-order [67] and intra-particle diffusion models [68], respectively given by Eqs. 6-8.

$$\ln(q_e - q_t) = \ln q_e - k_1 t \qquad (6)$$

$$\frac{t}{q_t} = \frac{1}{k_2 q^2} + \frac{t}{q_e} \qquad (7)$$

$$q_t = k_{\mathrm{id}} t^{\frac{1}{2}} + C \qquad (8)$$

where q_t indicates the adsorption at time (t) and q_e is the equilibrium adsorption capacity (mg g^{-1}). The adsorption rate constants for the pseudo first-order, pseudo second-order and intra-particle diffusion models are respectively represented by k_1 (min^{-1}), k_2 (g mg^{-1} min^{-1}) and k_{id} (mg g^{-1} $min^{0.5}$). The adsorption kinetics experiments were studied at 35°C and 0.4 g/40 mL adsorbent dose to find the adsorption equilibrium time at fixed initial DBT concentration. The equilibrium time was determined to be 100 min and no significant changes in the adsorption capacities were observed after that time (see Fig. S6). For the pseudo first-order (PFO) kinetic model (Eq. 6), the adsorption rate constant (k_1) and the amount of adsorbate at equilibrium (q_e) can be obtained from the slope and intercept of the linear plot shown in Fig. 13a and b. According to the coefficient of determination (R^2) values listed in Table 3, it can be concluded that the kinetics data for the wire-, rod-, and flower-like Fe_3O_4@MnO_2 NPs as well as the newly-synthesized magnetic nanoadsorbents are very well fitted by a pseudo first-order model. Furthermore, the experimental adsorption capacity (q_e exp.) is also in a very good agreement with the calculated adsorption capacity (q_e cal.) obtained from the pseudo first-order model. This suggests that the overall sulphur adsorption is most likely to be a mass transfer-controlled process [1].

In the case of pseudo second-order (PSO) kinetic model (Eq. 7), three steps are presupposed: firstly, the DBT molecules diffuse through the external film surrounding the adsorbent; then they diffuse

into the adsorbent pores; and ultimately they adsorb into the active sites *via* chemisorption [69]. The adsorption rate constant (k_2) and the amount of adsorbate at equilibrium (q_e) can be calculated from the slope and intercept of the linear plot shown in Fig. 13c and d. However, there was significant divergence between experimental and calculated adsorption capacities of DBT, and the R^2 values were slightly lower than those for the pseudo first-order model (see Table 4). The k_1 values obtained from PFO modelling were higher than the k_2 values obtained from the PSO model. This indicates that DBT removal by the prepared magnetic nanoadsorbents is more likely to occur *via* physisorption than chemisorption process.

To study the diffusion mechanism of DBT molecules into the adsorbent pores, the intra-particle diffusion model (Eq. 8) was used. According to this model, if intra-particle diffusion is involved in the adsorption process, then the plot of the (q_t) adsorbed at time t versus $t^{0.5}$ should be linear and pass through the origin (C = 0), where the parameter C represents the boundary layer effect (surface sorption) contribution [70]. As shown in Fig. 13e and f, as well as the values of k_{id}, C, and R^2 in Table 4, the regression line does not exactly pass through the origin (C ≠ 0) which indicates that intra-particle diffusion may not be the only rate-controlling step and other processes might be involved, i.e. some degree of boundary layer (surface sorption) control of the adsorption rate of DBT over magnetic nanoadsorbents [68]. However, the efficiency of the sulphur removal depends mainly on the adsorbent's textural properties such as surface area, pore volume, pore diameter and mesoporosity [71]. As shown in section 3.4, our novel magnetic nanoadsorbents with different MnO_2 morphologies (wire, rod and flower) exhibited diverse ADS performances toward organic sulphur compounds in both model and real fuels. The sequence of our magnetic nanoadsorbents from the highest to the lowest efficiency in sulphur removal under optimum conditions was as follows: Fe_3O_4@MnO_2-w and Fe_3O_4@MnO_2-w@AC > Fe_3O_4@MnO_2-r and Fe_3O_4@MnO_2-r@AC > Fe_3O_4@MnO_2-f and Fe_3O_4@MnO_2-f@AC. The surface analysis revealed that the magnetic nanoadsorbents with wire-like morphology i.e. Fe_3O_4@MnO_2-w and Fe_3O_4@MnO_2-w@AC had respectively S_{BET} values of 96 and 480 $m^2\ g^{-1}$, pore volume values of 0.3850 and 0.3526 $cm^3\ g^{-1}$, and pore diameter values of 8.26 and 10.5 nm, which were all higher in comparison with other magnetic nanoadsorbents having rod- and flower-like morphologies (see Table 1 and 2). The adsorption kinetics study clearly reveals that the Fe_3O_4@MnO_2-w and Fe_3O_4@MnO_2-w@AC magnetic nanoadsorbents have the highest adsorption rate constants and were fitted very well by the pseudo first-order model (see Table 4). Furthermore, the results obtained from the intra-particle diffusion model (see Table 5) showed that Fe_3O_4@MnO_2-w and Fe_3O_4@MnO_2-w@AC have the highest k_{id} and the lowest C values among other magnetic nanoadsorbents under study. This demonstrates that

Paper published in Fuel, Volume 340, 2023, 127523 https://doi.org/10.1016/j.fuel.2023.127523

the intra-particle diffusion i.e. diffusion of DBT molecules into adsorbent pores has a predominant effect on the sulphur removal efficiency, while boundary layer (surface sorption) effect comes next. However, the adsorption kinetics data obtained from the intra-particle diffusion model for Fe_3O_4@MnO_2-r, Fe_3O_4@MnO_2-r@AC, Fe_3O_4@MnO_2-f, and Fe_3O_4@MnO_2-f@AC magnetic nanoadsorbents showed higher values for the C parameter in comparison with Fe_3O_4@MnO_2-w and Fe_3O_4@MnO_2-w@AC. This indicates that the adsorption process of DBT by these nanoadsorbents involves multiple steps.

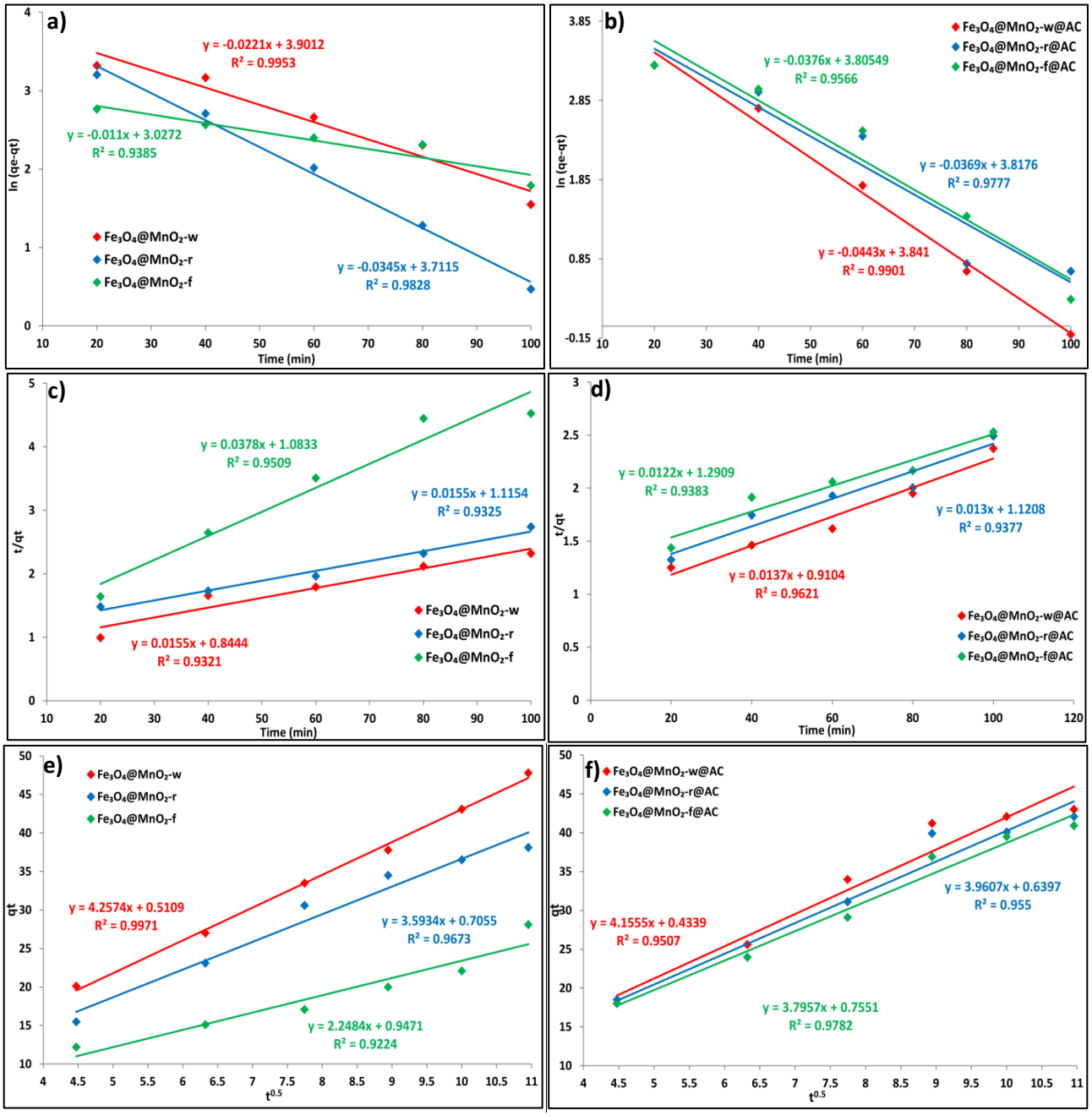

Fig. 13. Pseudo first-order kinetics (a and b); pseudo second-order kinetics (c and d); intra-particle diffusion (e and f) for the adsorption of DBT over wire-, rod-, flower-like Fe_3O_4@MnO_2 NPs and Fe_3O_4@MnO_2-w@AC, Fe_3O_4@MnO_2-r@AC and Fe_3O_4@MnO_2-f@AC magnetic nanoadsorbents.

Table 4: Kinetic parameters for DBT adsorption on wire-, rod- and flower-like Fe_3O_4@MnO_2 NPs, and magnetic nanoadsorbents.

	Pseudo first order kinetics				Pseudo second order kinetics		
Adsorbent	**qe exp (mg/g)**	**k_1 (min^{-1})**	**qe cal. (mg/g)**	**R^2**	**k_2 (g/mg. min)**	**qe cal. (mg/g)**	**R^2**
Fe_3O_4@MnO_2-w	47.8	0.0231	49.50	0.995	0.0183	64.51	0.932
Fe_3O_4@MnO_2-r	38.1	0.0317	40.91	0.982	0.0138	64.51	0.932
Fe_3O_4@MnO_2-f	28.1	0.0154	25.20	0.938	0.0348	26.45	0.950
Fe_3O_4@MnO_2-w@AC	43	0.03857	46.57	0.990	0.0145	73.52	0.963
Fe_3O_4@MnO_2-r@AC	42.1	0.03005	45.49	0.977	0.0115	76.92	0.937
Fe_3O_4@MnO_2-f@AC	40.9	0.02906	44.94	0.956	0.0094	81.96	0.938

Table 5: Intra-particle diffusion model calculations for DBT adsorption on wire-, rod- and flower-like Fe_3O_4@MnO_2 NPs, and magnetic nanoadsorbents.

Intra-particle diffusion model			
Adsorbent	**k_{id} (mg g^{-1} $min^{0.5}$)**	**C**	**R^2**
Fe_3O_4@MnO_2-w	3.729	0.5019	0.9971
Fe_3O_4@MnO_2-r	3.308	0.7055	0.9673
Fe_3O_4@MnO_2-f	2.085	0.9471	0.9224
Fe_3O_4@MnO_2-w@AC	4.557	0.4339	0.9507
Fe_3O_4@MnO_2-r@AC	4.330	0.6397	0.9550
Fe_3O_4@MnO_2-f@AC	4.303	0.7551	0.9782

3.6. Adsorption isotherms

The nature of adsorption of our magnetic nanoadsorbents was examined by utilizing the obtained adsorption data to various isotherm models, such as the Langmuir, Freundlich, and Temkin models using Eqs. 9-11 , respectively [72].

$$\frac{C_e}{q_e} = \frac{1}{k_L q_m} + \frac{C_e}{q_m} \qquad (9)$$

$$\ln q_e = \ln k_F + \frac{1}{n} \ln C_e \qquad (10)$$

$$q_e = \frac{RT}{B_T} \ln k_T + \frac{RT}{B_T} \ln C_e \qquad (11)$$

where C_e is the adsorbate concentration at equilibrium, q_e is the adsorption capacity (mg g^{-1}), q_m is the maximum monolayer coverage capacity (mg g^{-1}) and k_L is the Langmuir constant, which describes the relative affinity of the adsorbate. The adsorption capacity in the Freundlich model is denoted by k_F while the adsorption intensity is represented by n. For the Temkin model, k_T is the

Paper published in Fuel, Volume 340, 2023, 127523 https://doi.org/10.1016/j.fuel.2023.127523

equilibrium binding constant (L g^{-1}) and B_T is a constant associated with the heat of sorption (kJ mol^{-1}). The Langmuir model (Eq. 9) can precisely describe the monolayer adsorption (homogeneous surface) onto an adsorbent's surface with a finite number of adsorption sites. This model implies that there is uniform adsorption energy on the surface and that the adsorbate does not transmigrate in the plane of the surface [8]. The Langmuir isotherms of the prepared wire-, rod and flower-like Fe_3O_4@MnO_2 as well as the newly-synthesized Fe_3O_4@MnO_2-w@AC, Fe_3O_4@MnO_2-r@AC and Fe_3O_4@MnO_2-f@AC magnetic nanoadsorbents are shown in Fig. 14a,b, and the calculated parameters are provided in Table 6. The constant R_L presented in Table 5 is a dimensionless separation factor describing the adsorption mechanisms, which may be unfavourable (R_L > 1), linear (R_L = 1), favourable (0 < R_L < 1) or irreversible (R_L = 0) [6]. However, the data acquired from Langmuir isotherm analysis show that the adsorption mechanism is favourable for all the synthesized materials with R_L values less than unity. The fitting lines in Fig 14a reveal that the adsorption of DBT by wire-, rod- and flower-like Fe_3O_4@MnO_2 does not perfectly obey the Langmuir model especially with R^2 values far from unity. Whereas the Langmuir isotherms for the magnetic nanoadsorbents particularly Fe_3O_4@MnO_2-w@AC and Fe_3O_4@MnO_2-f@AC, confirmed the existence of homogeneous domains, uniform energies, and monolayer coverage with coefficient of determination R^2 values close to unity [67].

The Freundlich model (Eq. 10) describes the adsorption as a heterogeneous system. The Freundlich constants n and k_F can be calculated from the slope and intercept of the plot of ln qe versus ln Ce (see Fig. 14c and d). The obtained n values were larger than unity, highlighting that the adsorption of DBT over our magnetic nanoadsorbents could be multilayer physical adsorption, while the R^2 values close to unity indicate the validity of the experimental data with the Freundlich isotherm model [73].

The Temkin model implies that the heat of adsorption of DBT molecules drops linearly as the coverage of the adsorbent surface increases, and that adsorption is characterized by a uniform distribution of binding energies, up to a maximum value. The results shown in Fig. 14e and f and Table 6 indicate that DBT adsorption on our magnetic nanoadsorbents has the most exothermic energy (see B_T values in Table 6), suggesting that the most thermodynamically-favourable interaction occurs with these magnetic nanoadsorbents [25]. However, according to the R^2 values, the overall data fits follow the sequence: Freundlich model > Langmuir model > Temkin model. The higher R^2 values for Freundlich model than the other models reveal the porous and heterogeneous nature of our magnetic nanoadsorbents.

Paper published in Fuel, Volume 340, 2023, 127523 https://doi.org/10.1016/j.fuel.2023.127523

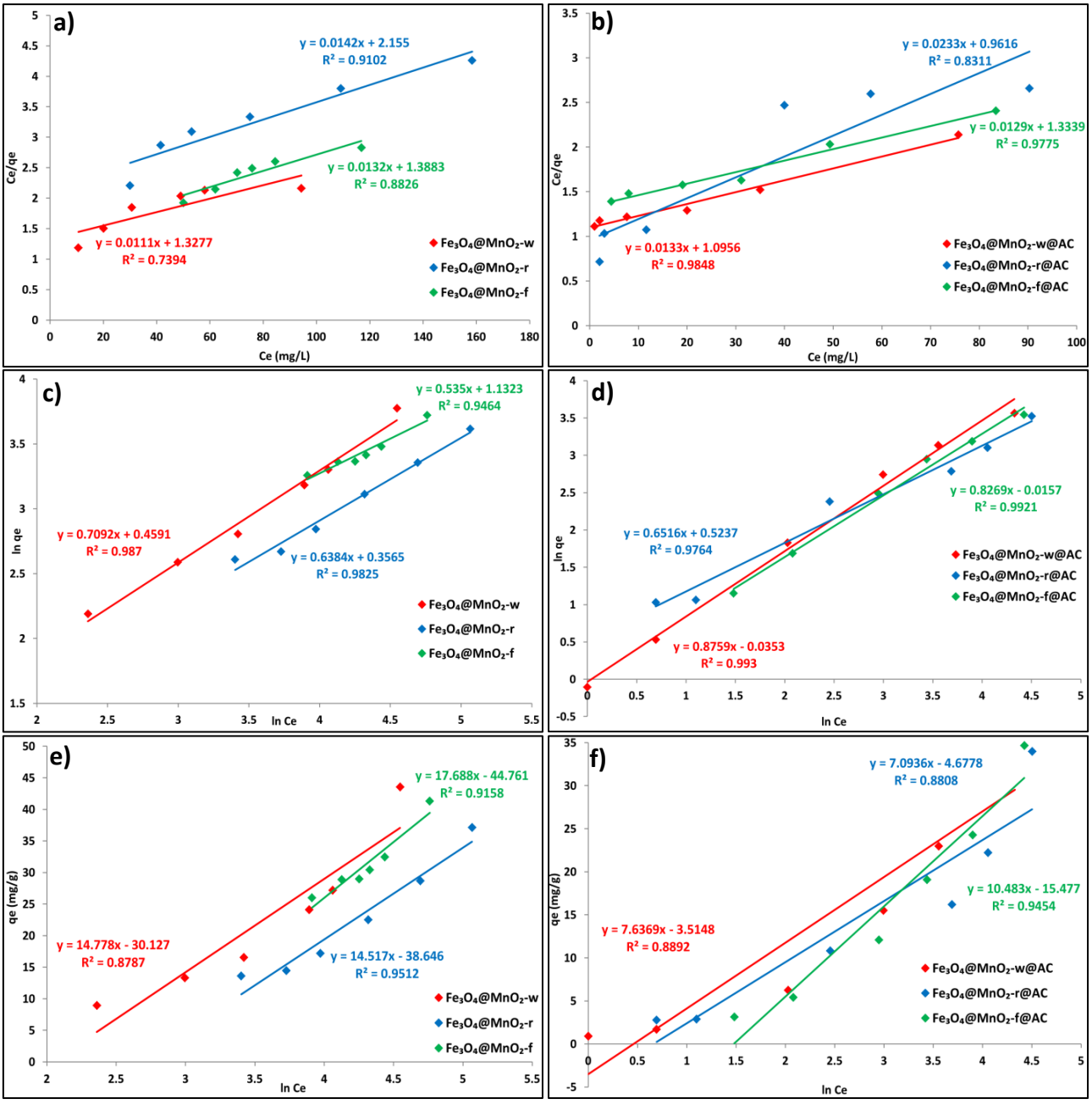

Fig. 14. DBT Adsorption isotherms: (a and b) Langmuir, (c and d) Freundlich and (e and f) Temkin

Table 6: Langmuir, Freundlich and Temkin parameters for adsorption of DBT on the prepared magnetic nanoadsorbents.

	Langmuir isotherm				Freundlich isotherm			Temkin isotherm		
Adsorbent	q_m (mg/g)	k_L (L/mg)	R^2	R_L	k_F (mg/g)	n	R^2	k_T (L/mg)	B_T kj/mol	R^2
Fe_3O_4@MnO_2-w	90.01	119.61	0.739	0.0095	1.58	1.41	0.987	0.130	14.77	0.878
Fe_3O_4@MnO_2-r	70.42	151.76	0.910	0.0031	1.42	1.56	0.982	0.068	14.50	0.951
Fe_3O_4@MnO_2-f	75.75	105.17	0.882	0.0024	3.10	1.86	0.946	0.079	17.68	0.915
Fe_3O_4@MnO_2-w@AC	75.18	82.37	0.984	0.4952	0.965	1.14	0.993	0.631	7.63	0.889
Fe_3O_4@MnO_2-r@AC	42.91	41.26	0.831	0.1444	1.688	1.53	0.976	0.517	7.09	0.880
Fe_3O_4@MnO_2-f@AC	77.51	103.47	0.977	0.1183	0.984	1.20	0.992	0.228	10.48	0.945

Paper published in Fuel, Volume 340, 2023, 127523 https://doi.org/10.1016/j.fuel.2023.127523

3.7. Adsorption thermodynamics

Thermodynamic parameters for adsorption of DBT on the new Fe_3O_4@MnO_2-w@AC, Fe_3O_4@MnO_2-r@AC and Fe_3O_4@MnO_2-f@AC magnetic nanoadsorbents were determined using experimental data obtained at different temperatures. Equilibrium adsorption constant k_e can be calculated *via* the expression in Eq. 11:

$$k_e = \frac{q_e}{C_e} \quad (11)$$

Gibbs free energy ΔG (kJ mol^{-1}) is expressed by Eq. 12:

$$\Delta G = -RT \ln k_e \quad (12)$$

where R is the gas constant, T is the absolute temperature and k is the equilibrium constant which varies with temperature as in Eq. 13:

$$\ln k_e = \frac{\Delta S}{T} - \frac{\Delta H}{RT} \quad (13)$$

where ΔS and ΔH are the entropy and enthalpy of adsorption, respectively [74].

The linear plots of ln k_e versus 1/T (see Fig. S7) for the DBT adsorption on the prepared magnetic nanoadsorbents indicate that the adsorption enthalpy and entropy changes were independent of temperature. The ΔH and ΔS were respectively calculated from the slopes and intercepts of these plots, and the obtained parameters are shown in Table 7. The adsorption of DBT from model oil was thermodynamically favourable and exothermic as indicated by the negative values of ΔG and ΔH at specific temperatures i.e. 25°C and 35°C [75]. However, a temperature above 45°C i.e. 60C°, renders the adsorption less favourable and shows an endothermic behaviour as indicated from the positive values of ΔG. Consequently, our prepared magnetic nanoadsorbents can perform ADS better at temperatures below 45°C. The negative values for ΔS indicate a decrease in the randomness upon DBT adsorption over the adsorbent surface. Furthermore, the calculated values of ΔG, ΔH, and ΔS confirm that the DBT adsorption is more favourable over Fe_3O_4@MnO_2-w@AC than on Fe_3O_4@MnO_2-r@AC and Fe_3O_4@MnO_2-f@AC magnetic nanoadsorbents. This is in very good agreement with the ADS results (see section 3.4) in the case of model and commercial fuel. The obtained ΔH values for our magnetic nanoadsorbents show that DBT-adsorbent interaction can be considered as enthalpy-driven, so the change in temperature can affect the adsorption process. However, the greater ΔH value for DBT adsorption may represent more unfavourable subsequent desorption. A subsequent desorption is necessary for regeneration and recycling of adsorbents. The thermodynamic studies demonstrated that our magnetic nanoadsorbents could be regenerated easily by a slight increase in temperature.

Paper published in Fuel, Volume 340, 2023, 127523 © 2023 Elsevier Ltd. https://doi.org/10.1016/j.fuel.2023.127523

The values of activation energy for the DBT adsorption on the prepared magnetic nanoadsorbents were calculated using the Arrhenius equation (Eq. 14) and kinetic data were obtained from the pseudo-first order model.

$$\ln k = -\frac{E_a}{RT} + \ln A \qquad (14)$$

where E_a is the activation energy of the adsorption process, which can be obtained from the slope of the linear plot of ln *k* versus 1/T (see Fig. S8), and A is the Arrhenius constant. All the calculated values were less than 40 kJ/mol (see Table 7), indicating that DBT adsorption by the magnetic nanoadsorbents occurred more readily, and that their adsorption processes were physical adsorption [76].

Table 7: Thermodynamic parameters for the adsorption process of DBT over the newly-prepared magnetic nanoadsorbents.

Adsorption thermodynamic parameters					
Adsorbent	**T °C (K)**	**ΔH kJ/mol**	**ΔS J/k/mol**	**ΔG kJ/mol**	**E_a kJ/mol**
Fe_3O_4@MnO_2-w@AC	25 (298) 35 (308) 45 (318) 60 (333)	-103.27	-317 -317 -317 -317	-8.70 -4.57 -2.35 2.40	12.40
Fe_3O_4@MnO_2-r@AC	25 (298) 35 (308) 45 (318) 60 (333)	-63.52	-200 -200 -200 -200	-3.70 -1.08 0.32 3.32	25.06
Fe_3O_4@MnO_2-f@AC	25 (298) 35 (308) 45 (318) 60 (333)	-52.47	-169 -169 -169 -169	-1.89 -0.31 1.50 4.04	28.13

3.8. Proposed mechanism for adsorption of DBT

The batch ADS experiments (Section 3.4), adsorption kinetics (Section 3.5), adsorption isotherms (section 3.6), and thermodynamic studies (Section 3.7), along with structural characterization (Sections 3.1-3.3), suggested that Fe_3O_4@MnO_2-w@AC, Fe_3O_4@MnO_2-r@AC, and Fe_3O_4@MnO_2-f@AC were effective magnetic nanoadsorbents for capturing organic sulphur from model and real fuels. Undecorated activated carbon had poorer ADS efficiency than the decorated ones i.e. Fe_3O_4@MnO_2-w@AC, Fe_3O_4@MnO_2-r@AC, and Fe_3O_4@MnO_2-f@AC; this implies that the incorporation of wire-, rod- and flower-like magnetic MnO_2 had created new active sites, which enhanced the adsorption of organic sulphur from model and real fuels. However, the kinetic studies and adsorption isotherms showed that the adsorption of DBT onto Fe_3O_4@MnO_2-w@AC with wire-like morphology depended primarily on DBT diffusion into the adsorbent pores. The BET studies for Fe_3O_4@MnO_2-w@AC showed a mesoporous structure with ink-bottle and slit-shaped pores [77]; the

calculated S_{BET} value was 480 m^2 g^{-1}, pore volume 0.3526 cm^3 g^{-1} and mean pore size 10.5 nm. The size of a DBT molecule (0.8 nm) is smaller than the pore diameter of Fe_3O_4@MnO_2-w@AC. The large specific surface area for wire-like magnetic nanoadsorbent provides more binding sites with ink-bottle and slit-shaped pores, thus allowing more DBT molecules to preferentially adsorb [78]. The smooth surface of the rod-like and the spherical shape with flower petals of the flower-like magnetic nanoadsorbents were less favourable for DBT removal than the wire-like morphology. The adsorption isotherms and thermodynamics for wire-like magnetic nanoadsorbent confirmed both mono- and multilayer DBT adsorption with minimum activation energy.

For flower-like δ-MnO_2, FESEM (Fig. 5e) revealed spherical shape (370-500 nm flowers estimated size) featuring flower petals interleaved with thin nanoplates (thickness 8-10 nm and length 37-45 nm), each of which appeared to grow perpendicularly from the inner core

Hence, the selective adsorption of DBT from fuels by the magnetic nanoadsorbents would be influenced by three key factors. Firstly, the size of DBT molecule is smaller than the adsorbent's pore diameters making it more easily trapped in the adsorbent. Secondly, the higher dipole moment, molar mass and aromaticity of DBT result in stronger van der Waals interactions with the magnetic nanoadsorbents. Thirdly, the higher basicity of DBT causes stronger acid-base interactions with magnetic manganese dioxide (Lewis acid) on the adsorbent surface [79]. A proposed mechanism is illustrated in Fig. 15.

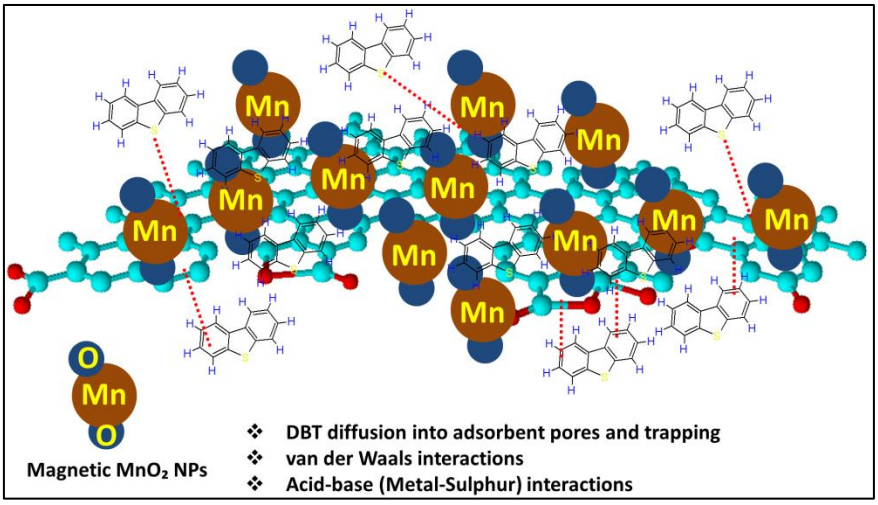

Fig. 15. Proposed mechanism for adsorption of DBT over synthesized magnetic nanoadsorbent

3.9. Regeneration and reusability

From the technological perspective, the useable lifetime of the nanoadsorbent is an essential parameter. Hence, the reusability of the best magnetic nanoadsorbent i.e. Fe_3O_4@MnO_2-w@AC was determined using model fuel under the optimized ADS process conditions. The regeneration process

Paper published in Fuel, Volume 340, 2023, 127523 © 2023 Elsevier Ltd. https://doi.org/10.1016/j.fuel.2023.127523

for the spent magnetic nanoadsorbent was done by Soxhlet extraction. Since chlorinated solvents are powerful in dissolving oil-based and organic substances [80], 150 mL dichloromethane (DCM) was utilized in the regeneration stage. The reusability of Fe_3O_4@MnO_2-w@AC magnetic nanoadsorbent (0.4 g) was studied over five cycles. After each run, the spent nanoadsorbent was regenerated by washing with DCM for 24h, followed by removing the residual solvent molecules on the adsorbent surface by drying at 100°C.

The first run with fresh magnetic nanoadsorbent showed 99% DBT removal after 100 min contact time (see Fig. 16). The DBT removal efficiency dropped to 97% after the first regeneration i.e. the second run, while a greater decline to 89% DBT removal was found when the adsorbent was reused for the fifth time (run no. 6). The progressive decrease in DBT removal efficiency may be due to some structural variations or loss of active sites during the regeneration process. Nevertheless, the high ADS performance (89%) of Fe_3O_4@MnO_2-w@AC magnetic nanoadsorbent after five times reuse make it a promising candidate for large-scale fuel processing without undue process costs.

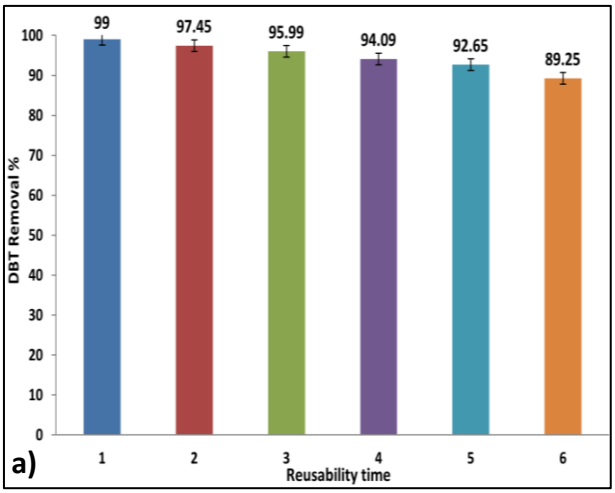

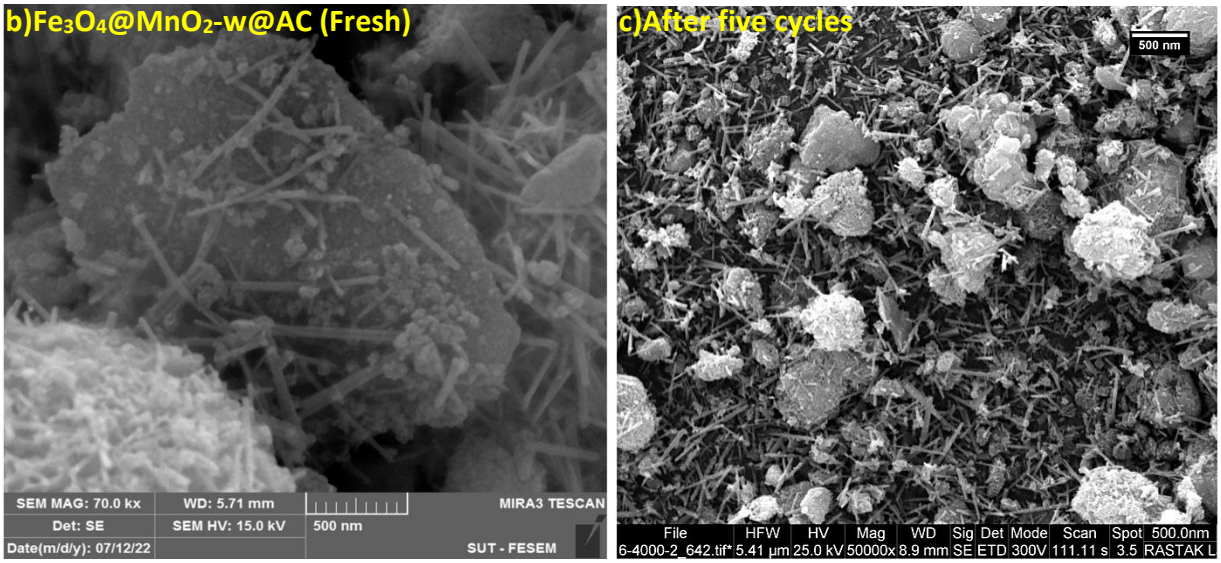

Fig. 16. (a): Reusability of Fe_3O_4@MnO_2-w@AC magnetic nanoadsorbent using model fuel, (b): FESEM micrograph of the fresh nanoadsorbent, (c): FESEM micrograph of the reusable nanoadsorbent after five cycles.

4. Conclusion

The present work reported the design and preparation of new magnetic nanoadsorbents with different morphologies and study of their performance in the ADS of model and commercial fuels under mild operating conditions. The hydrothermally synthesized magnetic nanoadsorbents were wire-, rod-, and flower-like Fe_3O_4@MnO_2-decorated activated carbons made from palm kernel shells. Structural characterization using FT-IR, XRD, EDAX elemental mapping, FESEM and TEM techniques confirmed the successful loading of wire-, rod- and flower-like Fe_3O_4@MnO_2 onto the AC. BET studies confirmed that the decoration process altered the porosity of the activated carbon, and that the newly-prepared magnetic nanoadsorbents had a mesoporous structure as well as high S_{BET} suitable for the adsorption of organic sulphur from model and real fuels. The adsorption kinetics of DBT by the prepared magnetic nanoadsorbents indicate a close match with the PFO kinetics, while adsorption isotherms analysed by Langmuir, Freundlich and Temkin models showed a surface with mono- and multilayer adsorption. Moreover, the intra-particle diffusion revealed that other mechanisms may play a role in the adsorption process, along with a mass-transfer mechanism. The adsorption thermodynamics demonstrated that the ADS process using our novel materials was thermodynamically favourable and exothermic in nature. The ADS experiments with model fuel revealed that the new magnetic nanoadsorbents performed best at 25-35°C adsorption temperature, 0.4 g adsorbent dose, 530 DBT concentration and 100 min contact time. The maximum DBT removal from model fuel was 99% for Fe_3O_4@MnO_2-w@AC, 95% for Fe_3O_4@MnO_2-r@AC and 93% for Fe_3O_4@MnO_2-f@AC. The ADS results for commercial kerosene were 97.6% for Fe_3O_4@MnO_2-w@AC, 93% for Fe_3O_4@MnO_2-r@AC, and 91% sulphur removal for Fe_3O_4@MnO_2-f@AC. The ADS results for commercial diesel fuel were 90% for Fe_3O_4@MnO_2-w@AC, 83.6% for Fe_3O_4@MnO_2-r@AC, and 73% sulphur removal for Fe_3O_4@MnO_2-f@AC under optimized ADS process conditions. Thus, utilizing these magnetic nanoadsorbents for sulphur removal could be technologically applicable, with the advantage of reusability for five times.

Acknowledgments

The authors are very grateful for the support offered by the School of Life Science, Pharmacy and Chemistry, Kingston University London. Special thanks go to the Industrial Chemistry Department, College of Science and Petroleum & Gas Refining Engineering Department, College of Petroleum Process Engineering, Tikrit University Iraq for their unlimited support.

Declaration of conflicting interests

The author(s) declared no potential conflicts of interest with respect to the research, authorship, and/or publication of this article.

Funding

The author(s) received no financial support for the research, authorship, and/or publication of this article.

ORCID iD

Omer Yasin Thayee Al-Janabi https://orcid.org/0000-0001-5435-112X

Peter J. S. Foot https://orcid.org/0000-0002-2122-3129

References

[1] A.M. Matloob, D.R. Abd El-Hafiz, L. Saad, S. Mikhail, D. Guirguis, Metal organic framework-graphene nano-composites for high adsorption removal of DBT as hazard material in liquid fuel, J. Hazard. Mater. 373 (2019) 447-458. https://doi.org/10.1016/j.jhazmat.2019.03.098.

[2] L.T. Abdulateef, A.T. Nawaf, O.Y.T. Al-Janabi, P.J.S. Foot, Q.A. Mahmood, Batch oxidative desulfurization of model light gasoil over a bimetallic nanocatalyst, Chem. Eng. Tech. 44 (2021) 1708-1715. https://doi.org/10.1002/ceat.202100027.

[3] H. Song, X. Li, B. Jiang, M. Gong, T. Hao, Preparation of novel and highly stable Py/MOF and its adsorptive desulfurization performance. Industr. Eng. Chem. Res. 58 (2019) 19586-19598. https://doi.org/10.1021/acs.iecr.9b02147.

[4] Y.Y. Liu, K. Leus, Z. Sun, X. Li, H. Depauw, A. Wang, P. Van Der Voort, Catalytic oxidative desulfurization of model and real diesel over a molybdenum anchored metal-organic framework, Micropor. Mesopor. Mater. 277 (2019) 245-252. https://doi.org/10.1016/j.micromeso.2018.11.004.

[5] M. Yaseen, S. Ullah, W. Ahmad, S. Subhan, F. Subhan, Fabrication of Zn and Mn loaded activated carbon derived from corn cobs for the adsorptive desulfurization of model and real fuel oils, Fuel. 284 (2021) 119102. https://doi.org/10.1016/j.fuel.2020.119102.

[6] T.A. Saleh, K.O. Sulaiman, S.A. AL-Hammadi, H. Dafalla, G.I. Danmaliki, Adsorptive desulfurization of thiophene, benzothiophene and dibenzothiophene over activated carbon manganese oxide nanocomposite: With column system evaluation, J. Clean. Prod. 154 (2017) 401-412. https://doi.org/10.1016/j.jclepro.2017.03.169 .

[7] X. Li, Y. Oska, L. Chen, L. Deng, H. Huang, Preparation of various manganese dioxide composites and their desulfurization performance, J. Energy Instit. 93 (2020) 1495-1502 https://doi.org/10.1016/j.joei.2020.01.011.

[8] Z. Zaidi, L.G. Sorokhaibam, Manganese modified multifunctional carbon material for desulfurization of transportation fuel and CO_2 sequestration, J. Environ. Chem. Eng. 9 (2021) 105378. https://doi.org/10.1016/j.jece.2021.105378.

[9] K.A.A. Safieh, Y.S. Al-Degs, M.S. Sunjuk, A.I. Saleh, M.A. Al-Ghouti, Selective removal of dibenzothiophene from commercial diesel using manganese dioxide-modified activated carbon: a kinetic study, Environ. Tech. 36 (2015) 98-105. https://doi.org/10.1080/09593330.2014.938125.

[10] J. Zhang, L. Wang, H. Song, H. Song, Adsorption of low-concentration H_2S on manganese dioxide-loaded activated carbon, Res. Chem. Intermed. 41 (2015) 6087-6104. https://doi.org/10.1007/s11164-014-1724-4.

[11] J. Zhang, G. Wang, W. Wang, H. Song, L. Wung, Preparation of manganese dioxide loaded activated carbon adsorbents and their desulfurization performance. Russ. J. Phys. Chem. 90 (2016) 2633-2641. https://doi.org/10.1134/S0036024416130100.

[12] J. Wang, Q. Zhang, H. Yang, C. Qiao, Adsorptive desulfurization of organic sulfur from model fuels by active carbon supported Mn (II): Equilibrium, Kinetics, and Thermodynamics, Int. J. Chem. Eng. 2020 (2020) 2813946. https://doi.org/10.1155/2020/2813946.

[13] J.A. Arcibar-Orozco, A.A. Acosta-Herrera, J.R. Rangel-Mendez, Simultaneous desulfurization and denitrogenation of model diesel fuel by Fe-Mn microwave modified activated carbon: Iron crystalline habit influence on adsorption capacity, J. Cleaner Prod. 218 (2019) 69-82. https://doi.org/10.1016/j.jclepro.2019.01.202.

[14] M.A. Al-Ghouti, Y.S. Al-Degs, Manganese-loaded activated carbon for the removal of organosulfur compounds from high-sulfur diesel fuels. Energy Tech. 2 (2014) 802-810. https://doi.org/10.1002/ente.201402033.

[15] M.A. Al-Ghouti, Y.S. Al-Degs, A.A. Issa, R.Z. Al Bakain, M.A. Khraisheh, Mechanistic and adsorption equilibrium studies of dibenzothiophene-rich-diesel on MnO_2-loaded-activated carbon: Surface characterization, Environ. Progr. Sustain. Energy. 36 (2017) 903-913. https://doi.org/10.1002/ep.12539.

[16] D.T. Tran, J.M. Palomino, S.R.J. Oliver, Desulfurization of JP-8 jet fuel: challenges and adsorptive materials, RSC. Adv. 8 (2018) 7301-7314. https://doi.org/10.1039/C7RA12784G.

[17] K.X. Lee, J.A. Valla, Adsorptive desulfurization of liquid hydrocarbons using zeolite-based sorbents: a comprehensive review, React. Chem. Eng. 4 (2019) 1357-1386. https://doi.org/10.1039/C9RE00036D.

[18] B. Saha, S. Sengupta, R. Selvin, Comparative studies of extraction ability of organic solvents to extract thiophene from model fuel, Sep. Sci. Technol. 55 (2020) 1123-1132. https://doi.org/10.1080/01496395.2019.1580292.

[19] L. Chen, Z.Y. Yuan, Design Strategies of Supported Metal-Based Catalysts for Efficient Oxidative Desulfurization of Fuel, J. Ind. Eng. Chem. 108 (2022) 1-14. https://doi.org/10.1016/j.jiec.2021.12.025.

[20] G. Mohebali, A.S. Ball, Biodesulfurization of diesel fuels - past, present and future perspectives, Int. Biodeterior. Biodegrad. 110 (2016) 163-180. https://doi.org/10.1016/j.ibiod.2016.03.011.

[21] I. Ahmed, S.H. Jhung, Composites of metal-organic frameworks: preparation and application in adsorption. Mater. Today. 7 (2014) 136-146. https://doi.org/10.1016/j.mattod.2014.03.002.

[22] J.M. Palomino, D. Tran, A. Kareh, C. Miller, J. Gardner, H. Dong, S. Oliver, Zirconia-silica based mesoporous desulfurization adsorbents. J. Power Sources 278, 141-148. https://doi.org/10.1016/j.jpowsour.2014.12.043.

[23] T.A. Saleh, G.I. Danmaliki, Adsorptive desulfurization of dibenzothiophene from fuels by rubber tyres-derived carbons: kinetics and isotherms evaluation. Process Saf. Environ. Prot. 102 (2016) 9-19. https://doi.org/10.1016/j.psep.2016.02.005.

[24] K.S. Triantafyllidis, E.A. Deliyanni, Desulfurization of diesel fuels: adsorption of 4,6-DMDBT on different origin and surface chemistry nanoporous activated carbons. Chem. Eng. J. 236 (2014) 406-414. https://doi.org/10.1016/j.cej.2013.09.099.

[25] A.A. Olajire, J.J. Abidemi, A. Lateef, N.U. Benson, Adsorptive desulphurization of model oil by Ag nanoparticles-modified activated carbon prepared from brewer's spent grains, J. Environ. Chem. Eng. 5 (2017) 147-159. http://dx.doi.org/10.1016/j.jece.2016.11.033.

[26] Y. Zu, Z. Guo, J. Zheng, Y. Hui, S. Wang, Y. Qin, L. Zhang, H. Liu, X. Gao, L. Song, Investigation of Cu(I)-Y zeolites with different Cu/Al ratios towards the ultra-deep adsorption desulfurization: discrimination and role of the specific adsorption active sites, Chem. Eng. J. 380 (2020) 122319. https://doi.org/10.1016/j.cej.2019.122319.

[27] R. Neubauer, M. Husmann, C. Weinlaender, N. Kienzl, E. Leitner, C. Hochenauer, Acid base interaction and its influence on the adsorption kinetics and selectivity order of aromatic sulfur heterocycles adsorbing on Ag-Al_2O_3, Chem. Eng. J. 309 (2017) 840-849. https://doi.org/10.1016/j.cej.2016.10.094.

[28] Z.C. Kampouraki, D.A. Giannakoudakis, V. Nair, A. Hosseini-Bandegharaei, J.C. Colmenares, E.A. Deliyanni, Metal organic frameworks as desulfurization adsorbents of DBT and 4,6-DMDBT from fuels, Molecules. 24 (2019) 1-23. https://doi.org/10.3390/molecules24244525.

[29] A. Mansouri, A.A. Khodadadi, Y. Mortazavi, Ultra-deep adsorptive desulfurization of a model diesel fuel on regenerable Ni-Cu/γ-Al2O3 at low temperatures in absence of hydrogen, J. Hazard. Mater. 271 (2014) 120-130. https://doi.org/10.1016/j.jhazmat.2014.02.006.

[30] S. Watanabe, X. Ma, C. Song, Adsorptive desulfurization of jet fuels over TiO_2- CeO_2 mixed oxides: role of Surface Ti and Ce cations, Catal. Today. 371 (2021) 265-275. https://doi.org/10.1016/j.cattod.2020.07.071.

[31] Y. Osaka, T. Kito, N. Kobayashi, S. Kurahara, H. Huang, H. Yuang, Z. He, Removal of sulfur dioxide from diesel exhaust gases by using dry desulfurization MnO_2 filter, Separ. Purif. Technol. 150 (2015) 80-85. https://doi.org/10.1016/j.seppur.2015.02.001.

[32] X. Liu, Y. Osaka, H. Huang, Huhetaoli, J. Li, X. Yang, S. Li, N. Kobayashi, Development of low-temperature desulfurization performance of MnO_2/AC composite for combined SO_2 trap from diesel exhaust, RSC. Adv. 6 (2016) 96367-96375. https://doi.org/10.1039/C6RA19017K.

[33] X. Liu, Y. Osaka, H. Huang, J. Li, Z. He, X. Yang, Huhetaoli, S. Li, N. Kobayashi, Development of a compact MnO_2 filter for removal of SO_2 from diesel vehicle emissions, RSC. Advances. 7 (2017) 18500-18507. https://doi.org/10.1039/C7RA00096K

[34] X. Duan, J. Yang, H. Gao, J. Ma, L. Jiao, W. Zheng, Controllable hydrothermal synthesis of manganese dioxide nanostructures: Shape evolution, growth mechanism and electrochemical properties, Cryst. Eng. Comm. 14 (2012) 4196-4204. https://doi.org/10.1039/C2CE06587H.

[35] T.A. Saleh, S. Agarwal, V.K. Gupta, Synthesis of MWCNT/MnO_2 and their application for simultaneous oxidation of arsenite and sorption of arsenate, Appl. Catal. B-Environ. 106 (2011) 46-53. https://doi.org/10.1016/j.apcatb.2011.05.003.

[36] A.L. Tiano, C. Koenigsmann, A.C. Santulli, S.S. Wong, Solution-based synthetic strategies for one-dimensional metal-containing nanostructures, Chem. Commun. 46 (2010) 8093-8130. https://doi.org/10.1039/C0CC01735C.

[37] B. Ming, J. Li, F. Kang, G. Pang, Y. Zhang, L. Chen, J. Xu, X. Wang, Microwave hydrothermal synthesis of birnessite-type MnO_2 nanospheres as supercapacitor electrode, J. Power Sources. 198 (2012) 428-431. https://doi.org/10.1016/j.jpowsour.2011.10.003.

[38] H. Jiang, T. Zhao, J. Ma, C. Yan, C. Li, Ultrafine manganese dioxide nanowire network for high-performance supercapacitors, Chem. Commun. 47 (2011) 1264-1266. https://doi.org/10.1039/C0CC04134C.

[39] D. Su, H.J. Ahn, G. Wang, Hydrothermal synthesis of αMnO_2 and βMnO_2 nanorods as high capacity cathode materials for sodium ion batteries, J. Mater. Chem. A. 1 (2013) 4845-4850. https://doi.org/10.1039/C3TA00031A.

[40] H. Jiang, T. Sun, C. Li, J. Ma, Hierarchical porous nanostructures assembled from ultrathin MnO_2 nanoflakes with enhanced supercapacitive performances, J. Mater. Chem. 22 (2012) 2751-2765. https://doi.org/10.1039/C1JM14732C.

[41] Y. Yang, C. Huang, Effect of synthetical conditions, morphology, and crystallographic structure of MnO_2 on its electrochemical behavior, J. Solid State Electrochem. 14 (2010) 1293-1301.

[42] K. Li, H. Li, T. Xiao, J. Long, G. Zhang, Y. Li, X. Liu, Z. Liang, F. Zheng, P. Zhang, Synthesis of manganese dioxide with different morphologies for thallium removal from wastewater, J. Environ. Management. 251 (2019) 109563. https://doi.org/10.1016/j.jenvman.2019.109563.

[43] R. Yang, Y. Fan, R. Ye, Y. Tang, X. Cao, Z. Yin, Z. Zeng, MnO_2-based materials for environmental applications, Adv. Mater. 33 (2021) 2004862. https://doi.org/10.1002/adma.202004862.

[44] H. Yang, M. Lu, D. Chen, R. Chen, L. Li, W. Han, Efficient and rapid removal of Pb^{2+} from water by magnetic Fe_3O_4@ MnO_2 core-shell nanoflower attached to carbon microtube: adsorption behaviour and process study, J. colloid and interface sci. 563 (2020) 218-228. https://doi.org/10.1016/j.jcis.2019.12.065.

[45] P. Maneechakr, S. Mongkollertlop, Investigation on adsorption behaviors of heavy metal ions (Cd^{2+}, Cr^{3+}, Hg^{2+} and Pb^{2+}) through low-cost/active manganese dioxide-modified magnetic biochar derived from palm kernel cake residue, J. Environ. Chem. Eng. 8 (2020) 104467. https://doi.org/10.1016/j.jece.2020.104467.

[46] M. Nozari, M. Malakootian, N.J.H. Fard, H. Mahmoudi-Moghaddam, Synthesis of Fe_3O_4@ PAC as a magnetic nano-composite for adsorption of dibutyl phthalate from the aqueous medium: Modeling, analysis and optimization using the response surface methodology. Surfaces and Interfaces. 31 (2022) 101981. https://doi.org/10.1016/j.surfin.2022.101981.

[47] M. Xu, L. Kong, W. Zhou, H. Li, Hydrothermal synthesis and pseudocapacitance properties of α-MnO_2 hollow spheres and hollow Urchins. J. Phys. Chem. C. 111 (2007) 19141-19147. https://doi.org/10.1021/jp076730b.

[48] E.J. Kim, C.S. Lee, Y.Y. Chang, Y.S. Chang, Hierarchically structured manganese oxide-coated magnetic nanocomposites for the efficient removal of heavy metal ions from aqueous systems. Appl. Mater. Interfaces. 5 (2013) 9628-9634. https://doi.org/10.1021/am402615m.

[49] A.F. Nicholas, M.Z. Hussein, Z. Zainal, T. Khadiran, Palm kernel shell activated carbon as an inorganic framework for shape-stabilized phase change material. Nanomaterials, 8 (2018) 689. https://doi.org/10.3390/nano8090689.

[50] X.R. Han, X.T. Guo, M.J. Xu, H. Pang, Y.M. Ma, Clean utilization of palm kernel shell: sustainable and naturally heteroatom-doped porous activated carbon for lithium–sulfur batteries, Rare Metals. 39 (2020) 1099-1106. https://doi.org/10.1007/s12598-020-01439-9.

[51] X. Liu, J. Wang, G. Yang, Amorphous nickel oxide and crystalline manganese oxide nanocomposite electrode for transparent and flexible supercapacitor, Chem. Eng. J. 347 (2018) 101-110. https://doi.org/10.1016/j.cej.2018.04.070.

[52] J. Jia, P. Zhang, L. Chen, The effect of morphology of α-MnO_2 on catalytic decomposition of gaseous ozone, Catal. Sci. Technol. 6 (2016) 5841-5847. https://doi.org/10.1039/C6CY00301J.

[53] F. Wang, H. Dai, J. Deng, G. Bai, K. Ji, Y. Liu, Manganese oxides with rod-, wire-, tube-, and flower-like morphologies: highly effective catalysts for the removal of toluene, Environ. Sci. Technol. 46 (2012) 4034-4041. https://doi.org/10.1021/es204038j.

[54] S. Chen, F. Xie, Selective adsorption of copper (II) ions in mixed solution by Fe_3O_4-MnO_2-EDTA magnetic nanoparticles. Appli. Surfac. Sci. 507 (2020) 145090. https://doi.org/10.1016/j.apsusc.2019.145090.

[55] M.L. Yeboah, X. Li, S. Zhou, Facile fabrication of biochar from palm kernel shell waste and its novel application to magnesium-based materials for hydrogen storage, Materials, 13 (2020) 625. https://doi.org/10.3390/ma13030625.

[56] C. Julien, M. Massot, R. Baddour-Hadjean, S. Franger, S. Bach, J.P. Pereira-Ramos, Raman spectra of birnessite manganese dioxides, Solid State Ionics. 159 (2003) 345-356. https://doi.org/10.1016/S0167-2738(03)00035-3.

[57] A.M. Jubb, H.C. Allen, Vibrational spectroscopic characterization of hematite, maghemite, and magnetite thin films produced by vapor deposition, ACS Appli. Mater. Interfac. 2 (2010) 2804-2812. https://doi.org/10.1021/am1004943.

[58] H. Li, X. Li, T. Xiao, Y. Chen, J. Long, G. Zhang, P. Zhang, C. Li, L. Zhuang, K. Li, Efficient removal of thallium (I) from wastewater using flower-like manganese dioxide coated magnetic pyrite cinder, Chem. Eng. J. 353 (2018) 867-877. https://doi.org/10.1016/j.cej.2018.07.169.

[59] R.F. Abdullah, U. Rashid, M.L. Ibrahim, B. Hazmi, F.A. Alharthi, I.A. Nehdi, Bifunctional nano-catalyst produced from palm kernel shell via hydrothermal-assisted carbonization for biodiesel production from waste cooking oil, Renewable and Sustainable Energy Reviews, 137 (2021) 110638. https://doi.org/10.1016/j.rser.2020.110638.

[60] P. Nuengmatcha, P. Porrawatkul, S. Chanthai, P. Sricharoen, N. Limchoowong, Enhanced photocatalytic degradation of methylene blue using Fe_2O_3/graphene/CuO nanocomposites under visible light, J. Environ. Chem. Eng. 7 (2019) 103438. https://doi.org/10.1016/j.jece.2019.103438.

[61] I.F. Waheed, O.Y.T Al-Janabi, P.J.S. Foot, Novel $MgFe_2O_4$-CuO/GO heterojunction magnetic nanocomposite: Synthesis, characterization, and batch photocatalytic degradation of methylene blue dye, J. Molec. Liq. 357 (2022) 119084. https://doi.org/10.1016/j.molliq.2022.119084.

[62] I.A. Al Zubaidy, F.B. Tarsh, N.N. Darwish, B.S.S.A. Majeed, A. Al Sharafi, L.A. Chacra, Adsorption process of sulfur removal from diesel oil using sorbent materials, J. Clean Energy Technologies. 1 (2013) 66-68. https://doi.org/10.7763/JOCET.2013.V1.16.

[63] D.S. Aribike, M.A. Usman, M.M. Oloruntoba, Adsorptive desulfurization of diesel using activated sewage sludge: kinetics, equilibrium and thermodynamics studies, Appl. Petrochem. Res. 10 (2020) 1-12. https://doi.org/10.1007/s13203-019-00239-2.

[64] T.A. Saleh, Simultaneous adsorptive desulfurization of diesel fuel over bimetallic nanoparticles loaded on activated carbon, J. Cleaner Prod. 172 (2018) 2123-2132, https://doi.org/10.1016/j.jclepro.2017.11.208

[65] M.M. Meimand, N. Javid, M. Malakootian, Adsorption of sulfur dioxide on clinoptilolite/nano iron oxide and natural clinoptilolite, Health Scope. 8 (2019) e69158. https://doi.org/10.5812/jhealthscope.69158.

[66] R. Martins, V. Vilar, R. Boaventura, Kinetic modelling of cadmium and lead removal by aquatic mosses, Braz. J. Chem. Eng. 31 (2014) 229-42. https://doi.org/10.1590/S0104-66322014000100021.

[67] M. Ozacar, I.A. Şengil, H. Turkmenler, Equilibrium and kinetic data, and adsorption mechanism for adsorption of lead onto valonia tannin resin, Chem. Eng. J. 143(2008) 32-42. https://doi.org/10.1016/j.cej.2007.12.005.

[68] B. Hameed, D. Mahmoud, A. Ahmad, Equilibrium modeling and kinetic studies on the adsorption of basic dye by a low-cost adsorbent: Coconut (Cocos nucifera) bunch waste, J. Hazard. Mater. 158 (2008) 65-72. https://doi.org/10.1016/j.jhazmat.2008.01.034.

[69] M. Claros, J. Kuta, O. El-Dahshan, J. Michalička, Y.P. Jimenez, S. Vallejos, Hydrothermally synthesized MnO_2 nanowires and their application in Lead (II) and Copper (II) batch adsorption, J. Mol. Liq. 325 (2021) 115203. https://doi.org/10.1016/j.molliq.2020.115203.

[70] S. Kurajica, I. Minga, R. Blazic, K. Muzina, P. Tominac, Adsorption and degradation kinetics of methylene blue on as-prepared and calcined titanate nanotubes, Athens J. Sci. 5 (2018) 7-22. https://doi.org/10.30958/ajs.5-1-1.

[71] B. Saha, S. Vedachalam, A.K. Dalai, Review on recent advances in adsorptive desulfurization, Fuel Process. Technol. 214 (2021) 106685. https://doi.org/10.1016/j.fuproc.2020.106685.

[72] N.F. Nejad, E. Shams, M.K. Amini, J.C. Bennett, Synthesis of magnetic mesoporous carbon and its application for adsorption of dibenzothiophene, Fuel Process. Technol. 106 (2013) 376-384. https://doi.org/10.1016/j.fuproc.2012.09.002.

[73] W. Yang, W. Zhou, W. Xu, Synthesis and characterization of a surface molecular imprinted polymer as a new adsorbent for the removal of dibenzothiophene, J. Chem. Eng. Data. 57 (2012) 1713-1720, https://doi.org/10.1021/je201380m.

[74] J. Wang, H. Liu, H. Yang, C. Qiao, Q. Li, Competition adsorption, equilibrium, kinetic, and thermodynamic studied over La (III)-loaded active carbons for dibenzothiophene removal, J. Chem. Eng. Data. 61 (2016) 3533-3541. https://doi.org/10.1021/acs.jced.6b00431.

[75] J. Wen, X. Han, H. Lin, Y. Zheng, W. Chu, A critical study on the adsorption of heterocyclic sulfur and nitrogen compounds by activated carbon: equilibrium, kinetics and thermodynamics, Chem. Eng. J.164 (2010) 29-36. https://doi.org/10.1016/j.cej.2010.07.068.

[76] L. Fei, J. Rui, R. Wang, Y. Lu, X. Yang, Equilibrium and kinetic studies on the adsorption of thiophene and dibenzothiophene onto NiCeY zeolite, RSC. Adv. 37 (2017) https://doi.org/10.1039/c7r00415j.

[77] H. Xia, Y. Wang, J. Lin, L. Lu, Hydrothermal synthesis of MnO_2/CNT nanocomposite with a CNT core/porous MnO_2 sheath hierarchy architecture for supercapacitors, Nanoscale Res. Lett. 7 (2012) 33. https://doi.org/10.1186/1556-276X-7-33.

[78] D. Jha, M.B. Haider, R. Kumar, N. Byamba-Ochir, W.G. Shim, B. Marriyappan Sivagnanam, H. Moon, Enhanced adsorptive desulfurization using Mongolian anthracite-based activated carbon. ACS omega. 4 (2019) 20844-20853. https://doi.org/10.1021/acsomega.9b03432.

[79] M.K. Nazal, M. Khaled, M.A. Atieh, I.H. Aljundi, G.A. Oweimreen, A.M. Abulkibash, The nature and kinetics of the adsorption of dibenzothiophene in model diesel fuel on carbonaceous materials loaded with aluminum oxide particles, Arabian J. Chem. 12 (2019) 3678-3691. https://doi.org/10.1016/j.arabjc.2015.12.003.

[80] K. Okawa, K. Suzuki, T. Takeshita, K. Nakano, Regeneration of granular activated carbon with adsorbed trichloroethylene using wet peroxide oxidation, Water Res. 41 (2007) 1045-1051. https://doi.org/10.1016/j.watres.2006.10.032.